Lubrication in the Ball and Socket Joint of a Swash Plate Mechanism

by

Catherine LiVolsi

Bachelor of Science in Mechanical Engineering, Bachelor of Arts in
Physics, University of Rhode Island (2015)

Submitted to the Department of Mechanical Engineering
in partial fulfillment of the requirements for the degree of

Master of Science in Mechanical Engineering

at the

MASSACHUSETTS INSTITUTE OF TECHNOLOGY

September 2020

Author . . . .
Department of Mechanical Engineering
August 6, 2020

Certified by. . . . .
Dr. Wai K. Cheng
Professor, Department of Mechanical Engineering
Thesis Supervisor

Accepted by . . . .
Professor Nicolas Hadjiconstantinou
Chairman, Committee for Graduate Students

Lubrication in the Ball and Socket Joint of a Swash Plate Mechanism

by

Catherine LiVolsi

Submitted to the Department of Mechanical Engineering
on August 6, 2020, in partial fulfillment of the
requirements for the degree of
Master of Science in Mechanical Engineering

Abstract

The tribology of the ball and socket on the connecting rod in a swash plate engine is studied in the hydrodynamic regime. The engine operates at $1390rpm$ with an axial load on the rod as high as $1 \times 10^4 N$. The instantaneous load and kinematics from a previous study for a swash plate engine was used as the input. The ball and socket were assumed to be smooth surfaces. Starting with Reynolds' equation in spherical coordinates, the pressure was solved for and integrated over the surface area of the socket to calculate the force exerted on the rod. This force was matched to the input load force by adjusting the ball-socket clearance using a search algorithm provided by the software MATLAB. The calculation proceeded until the minimum clearance point approached the oil hole; the oil hole did not support the pressure so that hydrodynamic lubrication failed. Then, the dissipated friction power due to hydrodynamic shear was calculated over the range of crank angles where hydrodynamic lubrication applied. Results show that the dissipated power is essentially negligible. The frictional coefficient is on the order of 1×10^{-4}. As the minimum clearance point approaches the oil hole, the clearance between the ball and socket comes within the asperity of the surfaces and there is a presence of boundary lubrication, which is outside the scope of the present study.

Thesis Supervisor: Dr. Wai K. Cheng
Title: Professor, Department of Mechanical Engineering

Acknowledgments

Contents

List of Figures

List of Tables

Chapter 1

Introduction

The concept of a swash plate mechanism was developed in the early 1900s by English inventor Anthony George Maldon Michell. Michell was an inventor specifically studying lubrication and bearing development; he successfully obtained several patents for hydrodynamic bearings. He developed his patent for the "Crankless Engine" in 1928 [1], which relied on contact "slippers" between the piston and the swash plate. The concept for application to automobiles did not become widely popular due to the amount of precision needed in manufacturing, even though the resulting engine was extremely compact and more efficient than the conventional crank engines at the time [2]. The tolerance needed for the design was uncommon for standard manufacturing processes and the benefits were not considered to be advantageous enough to warrant replacing established practices. The swash plate mechanism can most often be found in pumps, compressors, rotor systems, and occasionally engines.

Swash plate engines are used in applications that require compact packaging. Ball and socket joints appear in many physiological applications and mechanical devices. For the latter, an important application is in power transmission, for which a prime example is the swash plate mechanism. The mechanism uses the ball and socket joint to translate rotational motion into linear motion. The associated loads are much higher than what would be seen in biological applications. There has been much research and improvement on the ball and socket joint for physiological applications such as human joints, and the frictional forces are well defined. The amount of

research that has been done to characterise the frictional dissipation in a swash plate mechanism is sparse. This thesis is a study of the friction in a swash plate engine at the ball and socket joint. For this study, the geometry of the wobble plate engine was taken from Roberts [3], reference figure 1-1. The output mechanism of a swash plate engine consists of four main parts: the connecting rods to the pistons, the wobble plate, which holds a socket joint to the ball- end of each connecting rod, the swash plate, and the drive shaft. A kinematic study in chapter 3 describes the whole system in reference to a set of inertial coordinates. A dynamic analysis in chapter 4 incorporates the piston force and inertial forces into the overall forces acting on the ball and socket joint through the kinematics. The kinematics and dynamics were performed in conjunction with Roberts' work, [3]. The engine simulation that was created in Roberts' work was used to supply the loads and speeds associated with the ball and socket joint in this analysis.

Figure 1-1 shows a cross sectional view of the wobble plate and piston mechanism that was considered in this study. The swash plate (2) is keyed at an incline to the drive shaft (1), and rotates with the drive shaft. The wobble plate (4) is separated from the swash plate by a roller thrust bearing (3). The wobble plate is prevented from rotating about the drive shaft by the cam follower (5), which translates in a groove of the engine housing (not shown). The cam follower restricts the wobble plate movement to a linear up-and down motion as the drive shaft goes through a revolution.

For a 6-cylinder engine, there are six pistons connected to the wobble plate via the connecting rods using ball- and socket- joints. Each piston head (9) has a socket connecting to a ball joint, which is screwed to the connecting rod (8). The other end of the connecting rod is screwed to another ball joint (7) that interfaces with the wobble plate. Each ball joint on the wobble plate sits in a socket (6), which has a hole in the bottom face to allow for oil passage. It is desired to know and to characterize the friction and lubrication regime between the ball and socket joint. Characterizing the lubrication and frictional behavior in the ball/socket joint will aid the design of future engines. For smaller engines, the frictional force is significant, due to the
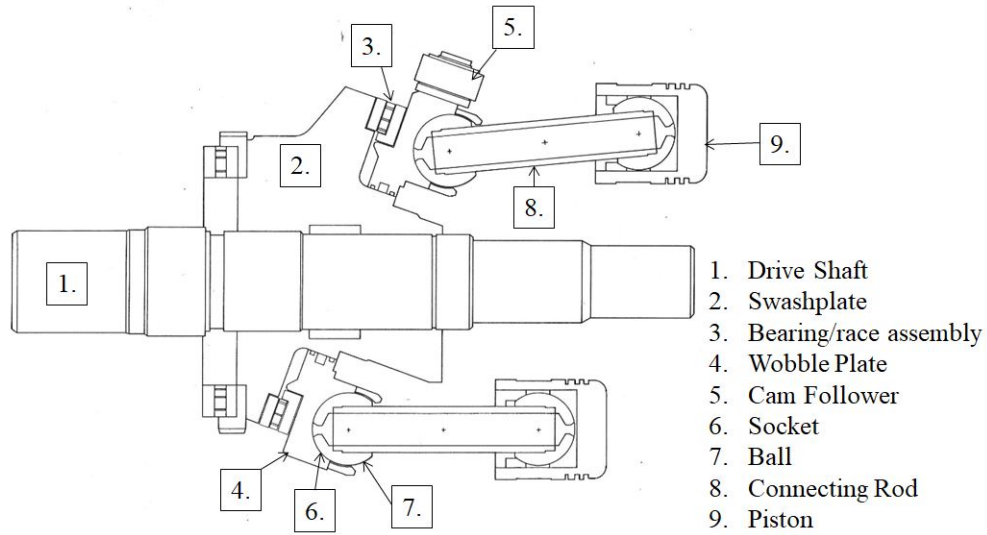
Figure 1-1: Swash Plate Engine Drive Line Assembly

1. Drive Shaft
2. Swashplate
3. Bearing/race assembly
4. Wobble Plate
5. Cam Follower
6. Socket
7. Ball
8. Connecting Rod
9. Piston

smaller size of the ball joint and corresponding higher stress level. In the following, a lubrication model was used to calculate the lubricant film thickness and associated friction in the ball/socket joint on the wobble plate.

Chapter 2

Lubrication Model

The lubrication film flow between the ball and the socket was formulated in spherical coordinates [4]. In the hydrodynamic lubrication regime, the Reynolds equation for an incompressible fluid is

$$
sin\theta\frac{\partial}{\partial\theta}(sin\theta\frac{h^3}{\mu}\frac{\partial P}{\partial\theta}) + \frac{\partial}{\partial\phi}(\frac{h^3}{\mu}\frac{\partial P}{\partial\phi}) - 6Rsin\theta[\frac{\partial}{\partial\theta}(sin\theta\cdot uh)
$$
$$
+ \frac{\partial}{\partial\phi}(vh)] - 12R^2sin^2\theta\frac{\partial h}{\partial t} = 0 \tag{2.1}
$$

Reference figure 2-1. Here, θ and ϕ are the polar and azimuthal angular coordinates; P is the local pressure; μ is the kinematic viscosity of the lubricant; and R is the radius of the socket. The relative velocities between the ball and socket are u and v respectively in the θ and ϕ directions.

The instantaneous relative velocity between the ball and socket was calculated from the angular velocity of the ball relative to the socket. The values for the relative angular velocity were supplied from the engine simulation by Roberts. The socket-to-ball clearance, h, was assumed to be small in comparison to R.

The $\frac{\partial}{\partial\theta}(sin\theta\cdot uh) + \frac{\partial}{\partial\phi}(vh)$ expression is interpreted as the "wedge" term representing the contribution of the relative tangential velocities; the $sin^2\theta\frac{\partial h}{\partial t}$ expression is interpreted as the "squeeze" term representing that of the relative normal velocity. Point O' in figure 2-1(a) is the center of the ball, and point O'' is the spherical center of the socket. The coordinate systems, $[X', Y', Z]$ and $[X'', Y'', Z'']$ are for the ball

17

and for the socket, respectively, and will be discussed further in chapter 3.

Point A is an arbitrary point on the spherical radius of the socket. Point B is the projection of point A on the $X'' - Y''$ plane, to show the angle ϕ measured from the X'' axis. $[\hat{e}_\theta, \hat{e}_R, \hat{e}_\phi]$ are the spherical unit vectors for the θ, R, and ϕ directions, respectively. Figure 2-1 is not drawn to scale. Figure 2-1(b) shows a cross-sectional view of the ball and socket joint, which is the interface between items (6) and (7) in figure 1-1. The variable, h, represents the film thickness. R_b and R_s are the radii of the ball and socket, respectively. The vector R shown in figure 2-1(a) is the average of the radii of the ball and socket, which will be discussed in chapter 5. The gap between the ball and socket illustrated in figure 2-1(b) is flooded with oil with viscosity μ. The center of the oil hole is shown as the gap in the socket, through which the Z'' axis passes.

(a) View 1 (b) View 2
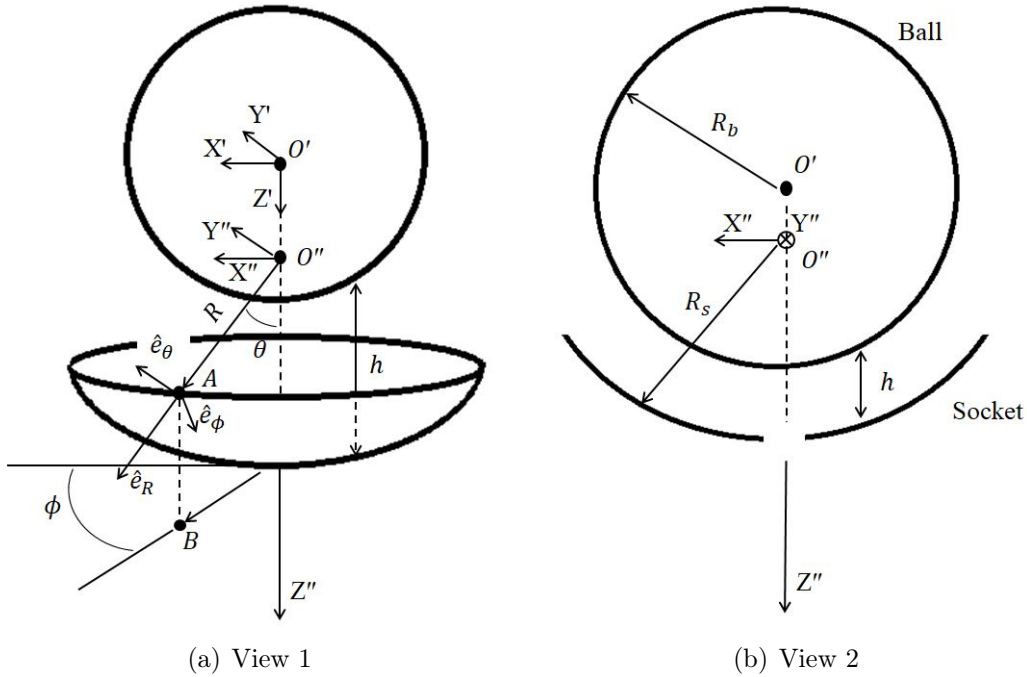
Figure 2-1: Nomenclature for Reynolds' Equation in Spherical Coordinates

The clearance between the ball and the socket was assumed to be fully flooded. The lubrication film thickness, h, was determined by the small offset of the center of the ball to the socket. The offset may be defined by an offset e_z in the axial direction, and a radial offset of e_r on an azimuthal plane at an azimuthal angle, ψ. Then, for

$h << R$, h was given by:

$$h = c - e_z cos\theta - e_r cos(\phi - \psi)sin\theta \qquad (2.2)$$

where c was the difference between the radii of the ball and the socket. The derivation of equation 2.2 is discussed in chapter 5, using general angles. Figure 2-2 illustrates an exaggerated eccentricity offset between the ball and socket. R_b and R_s are the radii of the ball and socket, respectively. The vector, $\vec{e}$, is composed of both the axial and radial eccentricities, e_z and e_r, offset at angle ψ. Figure 2-2(a) shows the center of the ball, point O', offset from the spherical center of the socket, point O''. Figure 2-2(b) shows the angular offset of the two centers, ψ, with reference to the socket coordinate system. The eccentricity parameter is discussed in more detail in chapter 5. Note that figure 2-2 is not drawn to scale.

(a) Radial and Axial Eccentricities   (b) ψ with Z'' axis into the page

Figure 2-2: Eccentricity

The value for h, defined by the value of the eccentricity parameters, $ecc = (e_z, e_r, \psi)$ was unknown. At each point in time, a guessed value for ecc was first used to find h. Then, from equation 2.1, $P(\phi, \theta, t)$ was found. The hydrodynamic

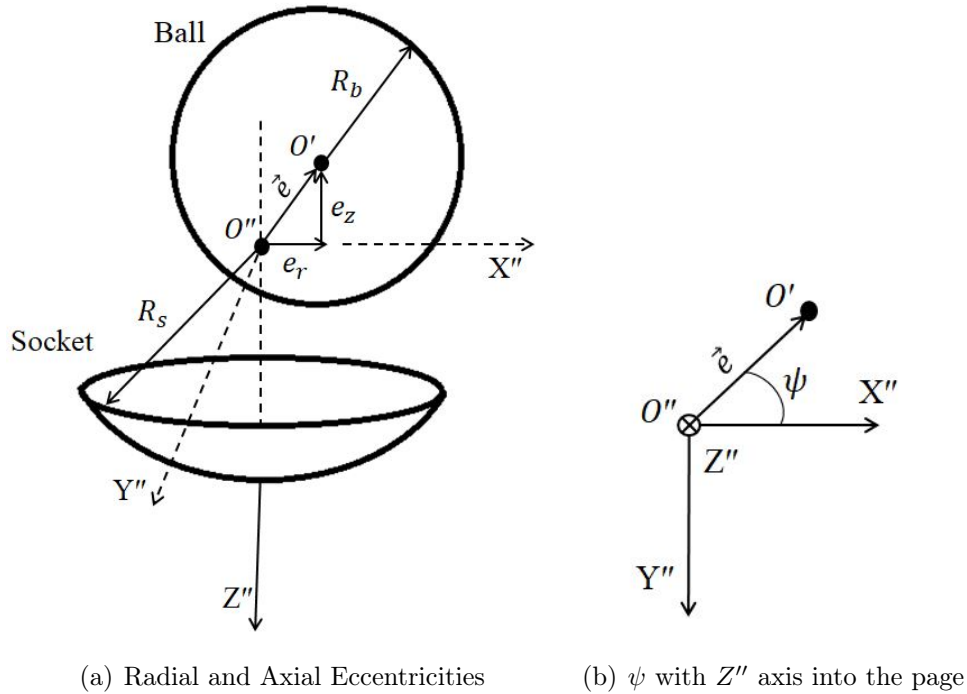forces, $\vec{F}$, in each direction created by the pressure field were calculated by the following equations:

$$F_x = R^2 \int_0^{2\pi} \int_{\theta_0}^{\frac{\pi}{2}} P(\phi,\theta,t) sin^2\theta cos\phi \, d\theta d\phi \qquad (2.3)$$

$$F_y = R^2 \int_0^{2\pi} \int_{\theta_0}^{\frac{\pi}{2}} P(\phi,\theta,t) sin^2\theta cos\phi \, d\theta d\phi \qquad (2.4)$$

$$F_z = R^2 \int_0^{2\pi} \int_{\theta_0}^{\frac{\pi}{2}} P(\phi,\theta,t) sin^2\theta cos\phi \, d\theta d\phi \qquad (2.5)$$

The applied force from Roberts' engine simulation in reference [3] was compared to the calculated forces from this dynamic analysis. If the values were not equal, the eccentricity vector was adjusted to calculate the film thickness, h, in equation 2.2. The pressure distribution in equation 2.1 was recalculated for use in equations 2.3, 2.4, and 2.5.

The domain for equation 2.1 was taken as $\theta_0 < \theta < \frac{\pi}{2}$ and $0 < \phi < 2\pi$. The value of θ_0 defined the boundary of the oil hole. The extent of the fully flooded region in the clearance was not known. The upper boundary of θ was set at the top of the ball seat cap, $\frac{\pi}{2}$. Since the movement of the connecting rod did not make a large inclination angle with respect to the socket, it was assumed that the high stress region was confined to the vicinity of the bottom oil hole. Therefore, the contribution to the overall friction for values of $\theta \gg \theta_0$ was not expected to be large.

The boundary conditions for Reynolds' equation for P in equation 2.1 were periodic in ϕ, with Dirichlet boundaries in θ.

$$\begin{array}{l|l} P = \text{Oil Pressure} & \theta = \theta_0 \\ P = \text{Crank Case Pressure} & \theta = \frac{\pi}{2} \end{array}$$

In addition to the oil hole at the bottom of the socket, there was another oil hole in the connecting rod ball to feed oil to the piston ball/socket joint. The most significant impact of this second hole on the ball/socket tribology was that the area formed by the union of the two holes coincided at the feed oil pressure, and therefore would not be able to support the joint load; the joint load required a high oil pressure.

Including this second hole in the model was complex because the geometry did not fit easily into the polar coordinates, and it was a function of time as the ball slid around the socket. Therefore, only the oil hole in the socket was accounted for in the current study. It was anticipated that the calculated ball-joint friction would thus be somewhat underestimated.

The model assumed full hydrodynamic lubrication throughout the entire domain of θ and ϕ. However, it was anticipated that at some point in the engine cycle the two surfaces would come into contact with each other. This would occur especially when the relative velocity between the ball and the socket was low, or when the position of the minimum ball-socket clearance approached the oil hole. The oil hole would not support high pressure; the lubrication film could break through ($h < 0$). The friction in the contact region depended on the deformation and roughness of the two surfaces, and its treatment was beyond the scope of this work and was left for future study.

Chapter 3

Kinematics

The kinematics were performed in conjunction with Roberts' engine simulation in reference [3]. The following is only a brief summary of the cited work, to provide context to the information provided by the engine simulation. A full description of the kinematics of the swash plate mechanism is included in the cited work.

3.1   Coordinate System Definition

Several coordinate systems were defined to analyze the kinematics of the system; the ball coordinate system (BCS), the socket coordinate system (SCS), the Wobble Plate Coordinate System (WPCS), and the Inertial Coordinate System (ICS). The relevant coordinate systems are shown in figure 3-1. It should be noted that the origins of the SCS and the BCS have a separation that is on the order of $(R_s - R_b) \sim 1 \times 10^{-5} m$.

The ICS z-axis, denoted Z, was defined as the centerline of the drive shaft, in the direction of the swash plate. The x-axis, X, was defined as perpendicular to Z and in the plane defined by the cam follower. The y-axis, Y, was dictated by the right hand rule:

$$\hat{Y} = \hat{Z} \times \hat{X}$$

The origin of the ICS was defined at the intersection of the centerline of the wobble plate and the z-axis.

The BCS and the SCS were defined relative to the ICS. The BCS z-axis, denoted Z', was along the centerline of the connecting rod in the direction of the wobble plate. The BCS x-axis, denoted X', was on the $Z - X$ plane and was perpendicular to Z'. The Y' axis was again dictated by the right-hand rule.

In a similar way, the origin of the SCS was at the spherical center of the socket. The z-axis of the socket, denoted Z'', was along the line connecting the centers of the socket and the oil hole, perpendicular to the surface of the wobble plate. The X'' axis was parallel to the centerline of the cam follower. Y'' was defined again by the right-hand rule.
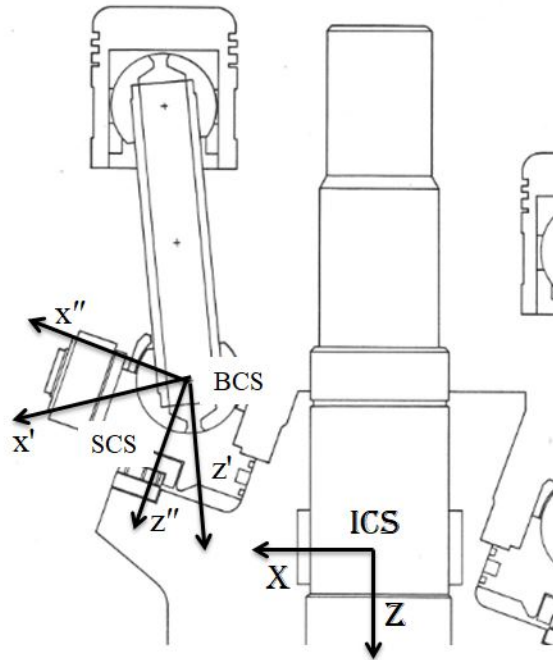
Figure 3-1: Coordinate Systems

From Roberts' engine simulation, the ICS was used to determine the relative velocity between the BCS and the SCS. A transformation matrix was derived that converted the BCS into the SCS via the ICS. The inertial forces associated with the components were calculated from the masses and the accelerations obtained from differentiating the velocities.

3.2 Transformation Matrices

Roberts' report identified transformation matrices that converted the WPCS to the ICS and the connecting rod coordinate system (CRCS) into the ICS. The CRCS and the BSC were parallel coordinate systems separated by a vector. This vector was accounted for in the conversion between coordinate systems.

It should be noted that transformation matrices are real and orthogonal, where for square matrix, A,

$$AA^T = I$$

where I is the identity matrix and A^T is the transpose of matrix A.

The transformation matrix to convert coordinates from the WPSC into the BCS was then derived in the following way:

Let the ICS be defined by $\hat{X}, \hat{Y}, \hat{Z}$ and the corresponding matrix be denoted $\hat{\Lambda}$. Similarly, the WPCS was defined $\hat{X}', \hat{Y}', \hat{Z}'$ and denoted $\hat{\lambda}$. The CRCS was defined $\hat{X}'', \hat{Y}'', \hat{Z}''$ and denoted $\hat{\mathcal{L}}$. Let $[\xi]$ be the transformation of WPCS into the ICS:

$$\hat{\Lambda} = [\xi]\hat{\lambda}$$
$$\hat{\lambda} = [\xi]^T\hat{\Lambda}$$

Let $[\sigma]$ be the transformation from CRCS into ICS:

$$\hat{\Lambda} = [\sigma]\hat{\mathcal{L}}$$

Using the definition of the ICS

$$\hat{\Lambda} = [\xi]\hat{\lambda}$$

$$[\sigma]\hat{\mathcal{L}} = [\xi]\hat{\lambda}$$

$$\hat{\mathcal{L}} = [\sigma]^T[\xi]\hat{\lambda}$$

$$\hat{\mathcal{L}} = [\mathbf{T}]\hat{\lambda}$$

where $[\mathbf{T}]$ was the transformation matrix from the WPCS into the CRCS, shown as $[\sigma]^T[\xi]$. The values of $[\sigma]$ and $[\xi]$ were calculated from Roberts' engine simulation in order to calculate $[\mathbf{T}]$. The angular velocity was calculated using the definition of a skew symmetric matrix, [5, 6].

$$\tilde{\omega} = [\dot{\mathbf{T}}][\mathbf{T}]^T \tag{3.1}$$

$$\vec{\omega} = \begin{bmatrix} \tilde{\omega}_{32} \\ \tilde{\omega}_{13} \\ \tilde{\omega}_{12} \end{bmatrix}$$

The linear velocities were calculated using the relationship

$$\vec{v} = \vec{\omega} \times \vec{R}$$

The output file of Roberts' engine simulation calculated both the transformation matrix and the angle between the z axes of the BCS and the SCS. The values contained in the output file of the engine simulation were in the reference frame of the CRCS. The transformation matrices were computed using the engine simulation provided by Roberts.

Chapter 4

Dynamics

A steady state analysis of the wobble plate was performed in Roberts' engine simulation. Newton's second law of motion and conservation of angular momentum were applied to each of the moving parts of the engine. The moving pieces were defined as each of the pistons, the connecting rod, the wobble plate, and the swash plate. The cylinder pressure applied a force to the face of the piston. This force was counteracted by the crankcase gas pressure applied to the opposite side of the piston, the cylinder wall friction, and the force applied by the connecting rod ball on the piston's ball seat. In general, the connecting rod was not co-linear with the cylinder's center line; thus the connecting rod applied a radial force on the piston's ball seat, which was counteracted by the cylinder wall. Using Newton's laws of motion and the known kinematics of the connecting rod, the reaction force at the opposite end of the connecting rod, point C in figure 4-1, was calculated. Point C was significant in this analysis as the forces that act at that point were used as the basis for calculating the eccentricity of the ball inside the socket. Figure 4-1 shows the Cartesian force vector on the connecting rod in the ICS, as defined in chapter 3. It should be noted that the forces on the ball, depicted in figure 4-1 as F_{Cx}, F_{Cy}, F_{Cz}, are in the BCS.

The force on the ball at point C originated from the wobble plate for every piston. The output results from the dynamic model of Roberts' engine simulation were read into a file. The data was presented in the BCS in Cartesian coordinates. The columns of the engine simulation output file are shown in table 4.1.
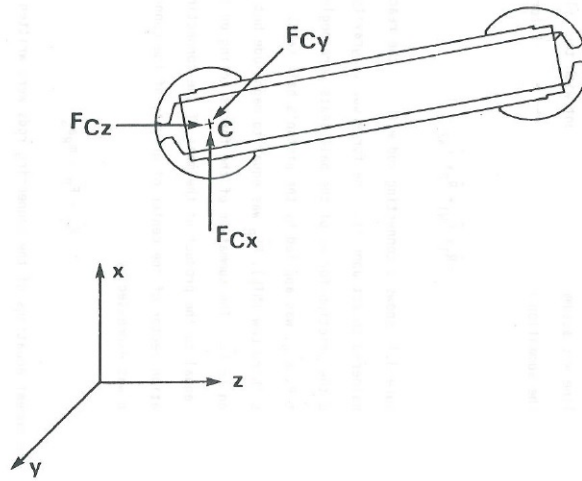
Figure 4-1: Dynamics on Connecting Rod, reprinted with author's permission from reference [3]. Forces are in BCS.

Row 2 was the crank angle of the swashplate, keyed to the drive shaft. Rows 3 through 5 in table 4.1 were the Cartesian force components acting on point C shown in figure 4-1. Rows 6 through 8 were the angular velocity components of the ball relative to the socket, discussed in chapter 3. T_{BtS} was as defined previously in chapter 3, the transformation matrix between the BCS and the SCS. Rows 9 through 17 were the matrix elements of the transformation matrix; the last element, $T_{BtS}(3,3)$, was the cosine of the angle between the z axis of the BCS and the z axis of the SCS. The values for the nomenclature shown in table 4.1 were used as the inputs to the numerical model, discussed in chapter 5, in order to solve for the dissipated friction between the ball and the socket on the surface of the wobble plate. Roberts' dynamic model yielded results for crank angles 0 - 360 degrees.

Column number	Nomenclature
1	Time (sec)
2	Crank Angle (Deg)
3	F_{Cx}(lbf)
4	F_{Cy}(lbf)
5	F_{Cz}(lbf)
6	$\omega_x(\frac{rad}{sec})$
7	$\omega_y(\frac{rad}{sec})$
8	$\omega_z(\frac{rad}{sec})$
9	$T_{BtS}(1,1)$
10	$T_{BtS}(1,2)$
11	$T_{BtS}(1,3)$
12	$T_{BtS}(2,1)$
13	$T_{BtS}(2,2)$
14	$T_{BtS}(2,3)$
15	$T_{BtS}(3,1)$
16	$T_{BtS}(3,2)$
17	$T_{BtS}(3,3)$

Table 4.1: File Format for Results from reference [3] Dynamic Analysis at Point C

Chapter 5

Numerical Analysis

In conjunction with Roberts' work, output from the kinematic and dynamic models of the engine simulation was saved to a file. This chapter discusses how the data from Roberts' engine simulation was utilized in order to solve for the frictional forces between the ball and socket joint in the swash plate mechanism. From here, the dissipated power was calculated to quantify the loss due to hydrodynamic lubrication.

Referencing table 4.1, the engine simulation output file contained columns of values for the Cartesian forces on the ball in each x, y, and z direction, linear velocities, and elements from the transformation matrix to convert between ball coordinates and socket coordinates for every crank angle from 0 to 360 degrees. The crank angle was given in increments of half degrees.

5.1   Initial and Reference Conditions

Full hydrodynamic lubrication was assumed. The parameters defining the problem are shown in 5.1.

P_{hole} was the pressure at the socket oil hole, P_{skirt} was the pressure at the film exit, R_b was the radius of the ball, R_s was the radius of the socket, R_{OH} was the radius of the oil hole, and μ was the viscosity of the oil. All calculations were performed with non-dimensionalized quantities. The reference quantities for non-dimensionalization were defined in table 5.2.

Parameter	Value
P_{hole}	0.5×10^6 Pa
P_{skirt}	1×10^5 Pa
R_b	0.9995 in
R_s	1.0001 in
R_{OH}	0.25 in
μ	$0.01 \frac{kg}{m-s}$

Table 5.1: Input Parameters

Nomenclature	Expression	Value
R_{ref}	$\frac{R_b + R_s}{2}$	2.54×10^{-2} m
h_{ref}	$R_s - R_b$	3.81×10^{-5} m
U_{ref}	$S_{shaft} R_{ref}$	3.692 m/sec
P_{ref}	$\frac{\mu U_{ref} R_{ref}}{h_{ref}^2}$	6.467×10^5 Pa

Table 5.2: Reference Parameters

S_{shaft} was the rotational speed of the drive shaft. This was calculated by taking the difference in crank angle divided by the time step. S_{shaft} was measured in $\frac{radians}{sec}$. All reference parameters were defined as global variables.

Equation 2.1 was non-dimensionalized using the parameters listed in table 5.2. The reference pressure was at first unknown, but was solved for in the following way:

$$h = h^* h_{ref}$$

$$R = R^* R_{ref}$$

$$u = u^* U_{ref}$$

$$v = v^* U_{ref}$$

$$t = t^* t_{ref}$$

$$t_{ref} = \frac{R_{ref}}{U_{ref}}$$

where all the starred values were non-dimensional values. Inserting these definitions of non-dimensional values into equation 2.1 yielded

$$h_{ref}^3 sin\theta \frac{\partial}{\partial\theta}(sin\theta \frac{h^{*3}}{\mu} \frac{\partial P}{\partial\theta}) + h_{ref}^3 \frac{\partial}{\partial\phi}(\frac{h^{*3}}{\mu} \frac{\partial P}{\partial\phi})$$

$$+ R_{ref} U_{ref} h_{ref}(-6R^* sin\theta[\frac{\partial}{\partial\theta}(sin\theta \dot{u}^* h^*) + \frac{\partial}{\partial\phi}(v^* h^*)])$$

$$- 12 \frac{R_{ref}^2 h_{ref}}{\frac{R_{ref}}{U_{ref}}} R^{*2} sin^2 \frac{\partial h^*}{\partial t^*} = 0$$

Factoring out $h_{ref} R_{ref} U_{ref}$ showed that the pressure should be non-dimensionalized with the term $\frac{\mu U_{ref} R_{ref}}{h_{ref}^2}$. For clarity, the superscript, $*$, will be neglected for all the non-dimensional variables in the subsequent discussion.

A finite difference model was defined using an $M \times N$ grid of 20 by 45 points distributed across the θ and ϕ directions respectively. In the θ direction, there were 20 points with Dirichlet pressure boundaries as defined in table 5.3. In the ϕ direction, there were 45 points with periodic pressure boundaries such that point $N + 1$ and point 1 were the same. The grid encompassed the following angular boundaries:

$$\theta_0 < \theta < \frac{\pi}{2}$$

$$0 < \phi < 2\pi$$

Pressure (Pa)	θ (radians)
$P = P_{hole}$	$\theta = \theta_0$
$P = P_{skirt}$	$\theta = \frac{\pi}{2}$

Table 5.3: Dirichlet Pressure Boundaries

θ_0 was defined as the angle corresponding to the edge of the oil hole. Referencing figure 5-1, $\theta_0 = arcsin(\frac{R_{OH}}{R_{ref}})$.

5.1.1 Eccentricity Parameter

Equation 2.2 showed how the film thickness, h, was calculated. This next section will show the derivation of the film thickness based on the eccentricity parameter. The eccentricity parameter for two offset spheres determined where the ball was positioned
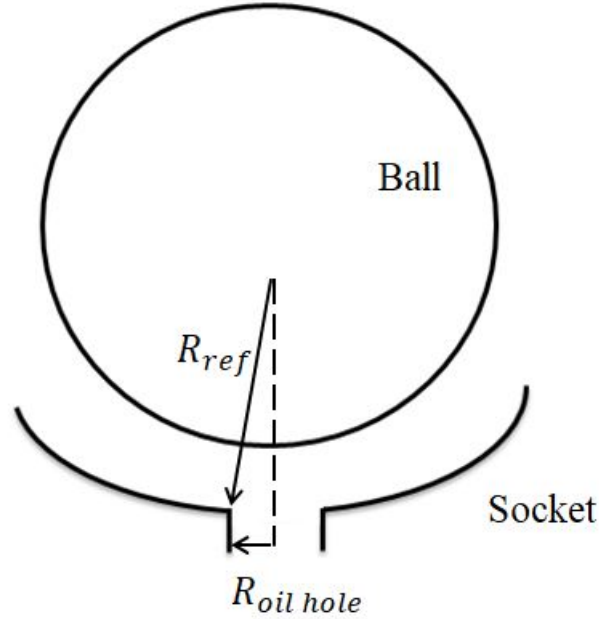
Figure 5-1: Calculation of θ_0

in the socket and was governed by three values $ecc = (e_z, e_r, \psi)$. The film thickness was defined as the layer of oil between the ball and socket and was governed by the eccentricity parameter. e_Z was the axial eccentricity, e_r was the radial eccentricity, and ψ was the angular offset. Reference figure 5-2, for some arbitrary center A in polar coordinates at angles δ and ξ on an arbitrary plane labeled P. The radial eccentricity was positioned on arbitrary plane Q at some angle ψ. The angle separating plane P from plane Q was given by $\xi - \psi$.

Calculating the eccentricity for just the z direction was done by setting the radial eccentricity equal to zero. Figure 5-3 shows two concentric spheres with their radial eccentricities aligned but offset in the z direction. The value of c was defined as the difference in the radii of the two spheres. From figure 5-3, the film thickness was calculated:

$$h = c - e_z \cos\delta \qquad (5.1)$$

Shown in figure 5-4 is the calculation of the film thickness if the center of the two spheres is offset in strictly the radial direction, and the centers align in the axial direction. Figure 5-4(a) shows two concentric spheres with the projection of e_r
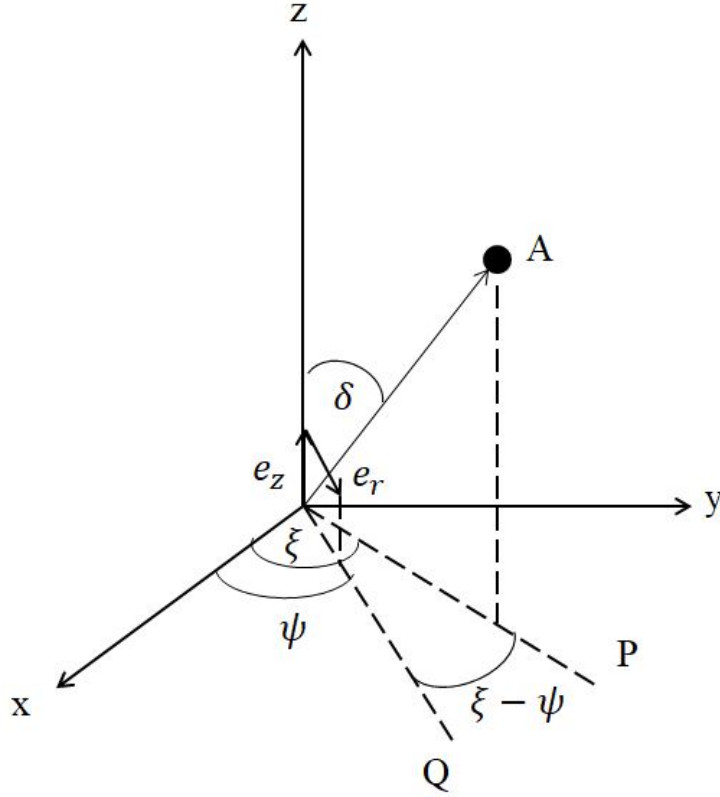
34

Figure 5-2: Eccentricity for any Arbitrary point A

onto the $z - P$ plane. Figure 5-4(b) shows the projection in context of the x, y, z coordinates.

Using figures 5-4(a) and 5-4(b), the film thickness was calculated:

$$h = c - e_r cos(\xi - \psi) sin\delta \qquad (5.2)$$

For the condition that $(h << R)$, the results from equation 5.2 and 5.1 could be combined together for a final solution to calculate the film thickness between two offset spheres as a function of angle and radii

$$h = c - e_z cos\delta - e_r cos(\xi - \psi) sin\delta \qquad (5.3)$$

Initial values for the eccentricity parameter were guessed with $\delta = 20°$, $e_z = 0.037$, from geometry $e_r = e_z tan(20°)$, and $\psi = \pi$. The initial values were somewhat
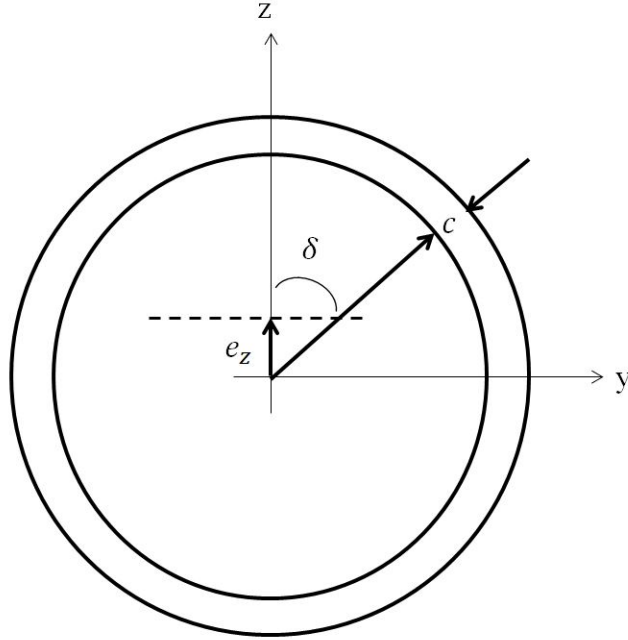
35

Figure 5-3: Eccentricity without e_r Offset

arbitrary, as will be explained in the subsequent sections; to facilitate convergence, the initial displacements were chosen in the direction of the force. The force vector acts at roughly 20 degrees from the vertical Z axis.

5.2 Velocity in polar coordinates

Initially the angular velocity was given in terms of the BCS in Cartesian coordinates. The Cartesian angular velocity was first converted to the SCS using the transformation matrix discussed in chapter 4, and then converted to polar coordinates using the transformation matrix, T_{CtP}:

$$T_{CtP} = \begin{bmatrix} sin\theta cos\phi & sin\theta sin\phi & cos\theta \\ cos\theta cos\phi & cos\theta sin\phi & -sin\theta \\ -\sin\phi & cos\phi & 0 \end{bmatrix}$$

The derivation of T_{CtP} matrix is shown in Appendix A.

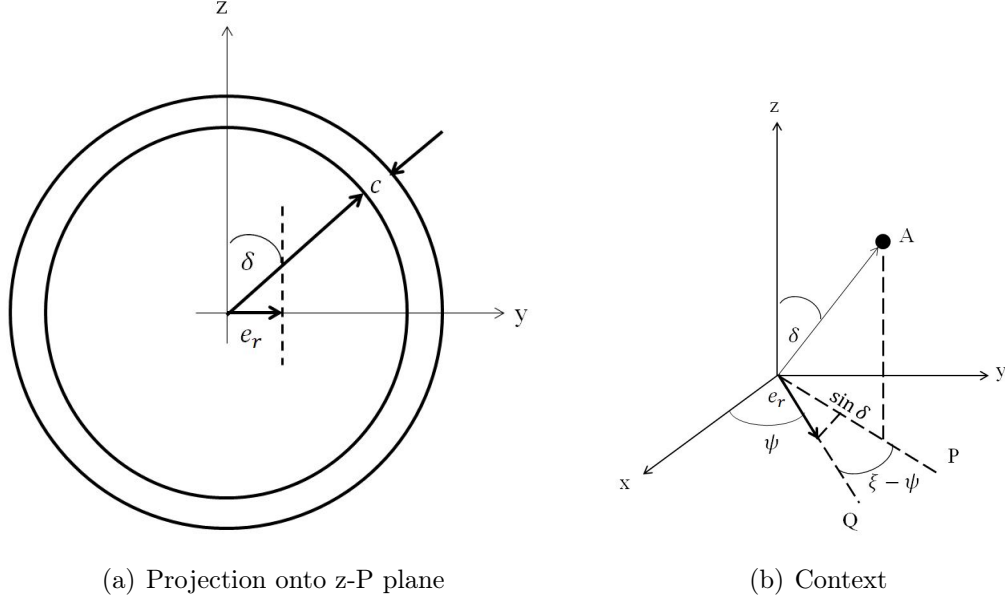(a) Projection onto z-P plane   (b) Context

Figure 5-4: Eccentricity without e_z Offset

The linear velocity was obtained by the cross product between the angular velocity and the radial vector.

$$\vec{v} = \vec{\omega} \times \vec{R}$$

Expanding the cross product for the three mutually perpendicular directions with $\vec{v} = [u\hat{e}_\theta, v\hat{e}_\phi, w\hat{e}_R]$, $\vec{\omega} = [\omega_\theta\hat{e}_\theta, \omega_\phi\hat{e}_\phi, \omega_R\hat{e}_R]$, and $\vec{R} = R\hat{e}_R$

$$u\hat{e}_\theta + v\hat{e}_\phi + w\hat{e}_R = (\omega_\theta\hat{e}_\theta + \omega_\phi\hat{e}_\phi + \omega_R\hat{e}_R) \times R\hat{e}_R \tag{5.4}$$

For the θ and ϕ directions respectively, equation 5.4 reduces to:

$$u = \omega_\phi R$$

$$v = -\omega_\theta R$$

where u is the velocity in the θ direction, and v is the velocity in the ϕ direction. This calculation was performed over the domain of both θ and ϕ to form $M \times N$ matrices for u and v.

5.3 Force

The force vector on the ball at point C in the BCS was a known value for each crank angle, discussed in chapter 4. The force was converted into the SCS by the transformation matrix, T_{BtS}, shown:

$$T_{BtS} = \begin{bmatrix} cos\zeta & 0 & -sin\zeta \\ 0 & 1 & 0 \\ sin\zeta & 0 & cos\zeta \end{bmatrix}$$

where ζ is defined in figure 5-5, the angle between the two z-axes of the BCS and SCS.
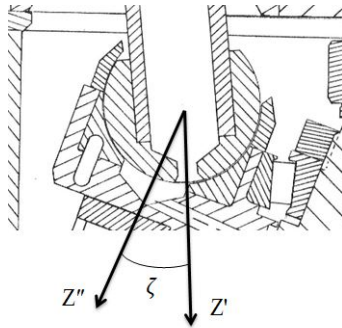

Figure 5-5: Angle between BCS and SCS z-axes

5.4 Poisson's Equation

The initial assumption for the pressure was a linear distribution between the two Dirichlet boundaries over the domain of θ and uniformly distributed over ϕ. This initial guess is immaterial as long as the solution converges quickly. The pressure was periodic over the domain of ϕ; for an $M \times N$ pressure matrix, the first column and the $N+1$ column were equal. The momentum balance on a fluid element in spherical coordinates, equation 2.1, is reproduced below:

$$sin\theta \frac{\partial}{\partial\theta}(sin\theta \frac{h^3}{\mu} \frac{\partial P}{\partial\theta}) + \frac{\partial}{\partial\phi}(\frac{h^3}{\mu} \frac{\partial P}{\partial\phi}) - 6Rsin\theta[\frac{\partial}{\partial\theta}(sin\theta \cdot uh)$$

$$+ \frac{\partial}{\partial\phi}(vh)] - 12R^2 sin^2\theta \frac{\partial h}{\partial t} = 0$$

Solving for the pressure distribution across both the θ and ϕ domain lies within a numerical simulation using a pseudo time step. To solve for the steady state pressure over the socket, the change in the pressure with respect to a differential pseudo time constant, τ, was set equal to the Reynolds equation and is shown in equation 5.5. The pseudo time serves as a measure to step through the Poisson solver and converge on a value for the pressure. Because the domain of θ does not include zero, $sin\theta$ was divided through equation 2.1.

$$\frac{\partial P}{\partial\tau} = \frac{\partial}{\partial\theta}(sin\theta \frac{h^3}{\mu} \frac{\partial P}{\partial\theta}) + \frac{1}{sin\theta} \frac{\partial}{\partial\phi}(\frac{h^3}{\mu} \frac{\partial P}{\partial\phi}) - Q \tag{5.5}$$

where

$$Q = 6R[\frac{\partial}{\partial\theta}(sin\theta uh) + \frac{\partial}{\partial\phi}(vh)] + 12R^2 sin\theta \dot{h}$$

Equation 2.1 can be expressed in terms of Poisson's equation:

$$\frac{\partial}{\partial\theta}(f \frac{\partial P}{\partial\theta}) + \frac{\partial}{\partial\phi}(g \frac{\partial P}{\partial\phi}) = Q \tag{5.6}$$

where

$$f = sin\theta \frac{h^3}{\mu}$$
$$g = \frac{1}{sin\theta} \frac{h^3}{\mu}$$

In this form, equation 5.6 could be solved more easily with finite differencing. The method of fractional steps [7] was employed for a combination of forward and

backward differencing in first the θ direction and then in the ϕ direction. Applying the method to equation 5.5 yielded:

$$\frac{P^{n+\frac{1}{2}} - P^n}{\frac{1}{2}\Delta\tau} = \frac{\partial}{\partial\theta}(sin\theta\frac{h^3}{\mu}\frac{\partial P^{n+\frac{1}{2}}}{\partial\theta}) + \frac{1}{sin\theta}\frac{\partial}{\partial\phi}(\frac{h^3}{\mu}\frac{\partial P^n}{\partial\phi}) - Q \qquad (5.7)$$

$$\frac{P^{n+1} - P^{n+\frac{1}{2}}}{\frac{1}{2}\Delta\tau} = \frac{\partial}{\partial\theta}(sin\theta\frac{h^3}{\mu}\frac{\partial P^{n+\frac{1}{2}}}{\partial\theta}) + \frac{1}{sin\theta}\frac{\partial}{\partial\phi}(\frac{h^3}{\mu}\frac{\partial P^{n+1}}{\partial\phi}) - Q \qquad (5.8)$$

In general, for any function $y = f(x)$, a second order approximation in Δx can be written in the following form:

$$\frac{\partial}{\partial x}(f\frac{\partial y}{\partial x}) = \frac{f\frac{\partial y}{\partial x}_{i+\frac{1}{2}} - f\frac{\partial y}{\partial x}_{i-\frac{1}{2}}}{\Delta x}$$
$$= (\frac{f_i + f_{i+1}}{2})(\frac{y_{i+1} - y_i}{\Delta x^2}) - (\frac{f_i + f_{i+1}}{2})(\frac{y_{i+1} - y_i}{\Delta x^2}) \qquad (5.9)$$

This general method was applied to equations 5.7 and 5.8 separately, for each θ and ϕ directions. Each direction was solved independently. A full description of the process is given in Appendix B. Once expressed in terms of the form shown in equation 5.9, the terms were collected and shown in the following form using the Thomas Method [8]:

$$-A_i y_{i+1} + B_i y_i - C_i y_{i-1} = D_i \qquad (5.10)$$

where $y = P_{i,j}^{n+\frac{1}{2}}$. Substitutions and definitions of each term are shown in Appendix B. Equation 5.10 is defined for $i = 2, \ldots, M - 1$. Inserting the known Dirichlet boundary conditions, equation 5.10 can be represented in matrix form:

$$\begin{bmatrix} 1 & 0 & 0 & \ldots & & 0 \\ 0 & -C_2 & B_2 & A_2 & \ldots & 0 \\ 0 & \ddots & \ddots & & & \\ \vdots & & -C_{M-1} & B_{M-1} & A_{M-1} \\ 0 & 0 & \ldots & & 1 \end{bmatrix} \begin{bmatrix} y_1 \\ y_2 \\ y_3 \\ \ldots \\ y_{M-1} \\ y_M \end{bmatrix} = \begin{bmatrix} y_1 \\ D_2 \\ D_3 \\ \ldots \\ D_{M-1} \\ y_M \end{bmatrix}$$

With a sparse matrix, S_θ, being defined as

$$
S_\theta =
\begin{bmatrix}
1 & 0 & 0 & \cdots & & 0 \\
0 & -C_2 & B_2 & A_2 & \cdots & 0 \\
0 & & \ddots & \ddots & & \\
\vdots & & & -C_{M-1} & B_{M-1} & A_{M-1} \\
0 & & 0 & \cdots & & 1
\end{bmatrix}
$$

The pressure in the θ direction can be solved for using the MATLAB matrix solver, since the equation can be written in the form of $Ax = b$. The same process is followed for the ϕ direction, utilizing the method of fractional steps and the Thomas Method. Because of the periodic boundary conditions in ϕ, the sparse matrix becomes:

$$
S_\phi =
\begin{bmatrix}
b_1 & -a_1 & 0 & \cdots & & -c_1 \\
-c_2 & b_2 & a_2 & 0 & & \cdots \\
0 & \ddots & \ddots & \ddots & & 0 \\
\vdots & & \ddots & \ddots & & \ddots \\
0 & & -c_{N-1} & b_{N-1} & -a_{N-1} & \\
-a_N & & & -c_N & b_N &
\end{bmatrix}
$$

The definitions of a_n, b_n, c_n are defined in Appendix B. The method of solving a sparse matrix with periodic boundary conditions can be found in reference [9]. S_ϕ has dimensions of $N \times N$. Similarly, the pressure in the ϕ direction can be solved using the form of $Ax = b$. The pressure in both the ϕ and θ directions was solved for by building the $M \times N$ matrix.

Initially, the pressure was assumed to be an even distribution between the two Dirichlet boundaries over the domain of θ. For each pseudo time step, the non-dimensional, calculated pressure from the Poisson solver was compared to the initial assumption. The relative error between the calculated value and the assumed value was restricted to below 1×10^{-4}. The Poisson solver iterated until the calculated error was below this value.

Once the pressure had converged, the pressure was integrated over the surface area

of the socket in order to solve for the force the socket applies on the ball using the trapezoidal rule. The integrated pressure gave a force in polar coordinates, and was converted into Cartesian coordinates using the inverse of the transformation matrix, T_{CtP}. The resulting force was converted into reference quantities with the reference pressure and the square of the reference length. The calculated force was then compared to the force collected from Roberts' dynamic model of the engine acting on point C in the center of the ball. The error between the two force values was not linear with respect to the eccentricity parameters; in order for the two force vectors to converge, the MATLAB function fsolve was used to solve the non-linear equation to determine the eccentricity parameters. The first element of the eccentricity parameter is the clearance between the ball and socket, e_z. As stated prior, the eccentricity vector was initially given an approximate value of $ecc = (e_z, e_r, \psi) = (0.037, 0.037 tan(20°), \pi)$. The initial values of the eccentricity parameter are somewhat arbitrary in that the program will eventually solve for the vertical and radial displacements, e_z and e_r; however, the initial assumptions must be close enough such that the program will be able to find a solution. The initial values were decided after running the program and allowing it to calculate the eccentricity parameter several times. Values that were approximately equal to these calculations were chosen to decrease convergence time. The film thickness, h, was recalculated according to equation 5.3 and the Poisson solver was rerun to find the new pressure at the corresponding film thickness. The pressure was again integrated over the area to solve for the new force and compared to the given force from the dynamic analysis. This comparison iteration was repeated until the calculated force from the Poisson solver converged with the force from the dynamic model. In this way the minimum clearance between the ball and socket was solved for each crank angle.

5.5   Dissipated Power

After the pressure distribution across the socket was solved for, the power dissipation due to friction was determined.

The friction power is shown below, in Watts:

$$\dot{W}_f = (\frac{h_{ref}}{R_{ref}})u_{ref}P_{ref}\int_0^{2\pi}\int_{\theta_0}^{\frac{\pi}{2}}(R_{ref}^2 sin\theta)[\frac{hu}{2R}(\frac{\partial P}{\partial \theta}) + \frac{u^2}{h} \\ + \frac{hv}{2Rsin\theta}(-\frac{\partial P}{\partial \phi}) + \frac{v^2}{h}]d\theta d\phi \tag{5.11}$$

The derivation is shown in Appendix C. $\dot{W}_f$ is defined as the power dissipated from the shear force of the lubrication. Because the initial assumption was fully hydrodynamic lubrication, the calculated dissipation was very low. For convenience, equation 5.11 was broken into four pieces:

$$\dot{W}_1 = \frac{hu}{2R}\frac{\partial P}{\partial \theta}$$
$$\dot{W}_2 = \frac{u^2}{h}$$
$$\dot{W}_3 = \frac{hv}{2Rsin\theta}\frac{\partial P}{\partial \phi}$$
$$\dot{W}_4 = \frac{v^2}{h}$$
$$C = (\frac{H_{ref}}{R_{ref}})U_{ref}P_{ref}R_{ref}^2$$

With these substitutions, equation 5.11 was rewritten as

$$\dot{W}_f = C\int_0^{2\pi}\int_{\theta_0}^{\frac{\pi}{2}}sin\theta(\dot{W}_1 + \dot{W}_2 + \dot{W}_3 + \dot{W}_4)d\theta d\phi$$

$\dot{W}_1$ and $\dot{W}_2$ are the terms associated with the shear force in the θ direction from Poiseuille and Couette flow, respectively. $\dot{W}_3$ and $\dot{W}_4$ are the terms associated with the shear force in the ϕ direction from Poiseuille and Couette flow, respectively.

Chapter 6

Results

From the output file, the forces on the ball at point C were tabulated. The force on the ball in the socket coordinate system was converted into Newtons and plotted, as shown in figure 6-1. Figures 6-1(a), 6-1(b), and 6-1(c) are plots of the forces in the X'', Y'', and Z'' directions respectively, against the crank angle. Figure 6-1(d) is the force vector on point C in the SCS, and was calculated $F_C = \sqrt{F_{X''}^2 + F_{Y''}^2 + F_{Z''}^2}$. As is shown in the figure, the force in the Z'' direction is the dominating force on the ball. The Z'' direction is along the centerline of the oil hole in the socket. A grid of 20 by 45 was chosen for the simulation with a pseudo time step equal to 0.01.

Referencing figure 6-1, only the crank angles that correspond to the maximum force were considered in the next section. The crank angles of interest were chosen to be between 250 degrees and 15 degrees. The piston is at top dead center at 0 degrees or 360 degrees; it is at bottom dead center at 180 degrees. This degree range was chosen as it is where there is significant force exerted on the socket, shown in figure 6-1(d). The ball starts with virtually no load, and progresses to maximum load. The calculation is not valid beyond 7 degrees because the clearance becomes negative, as shown in figure 6-2. Furthermore, in early compression (250-325 degrees) where the load is low and clearance is high, the solution is not valid because the pressure in some region of the domain becomes negative, which implies cavitation. Fortunately, that does not materially impact the subsequent solution because for the solution, the only memory of the previous time is through the squeeze term, which is small when the
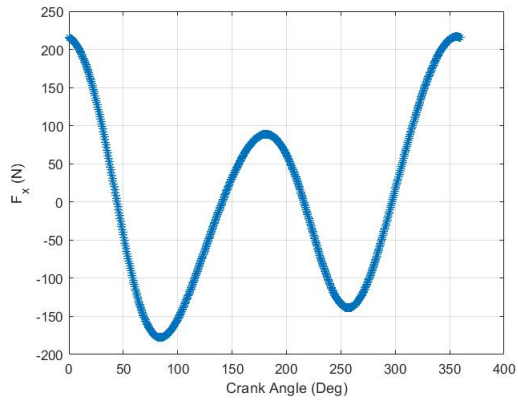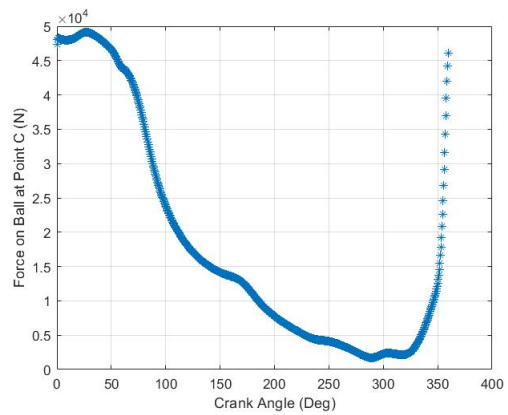
(a) $F_{X''}(N)$
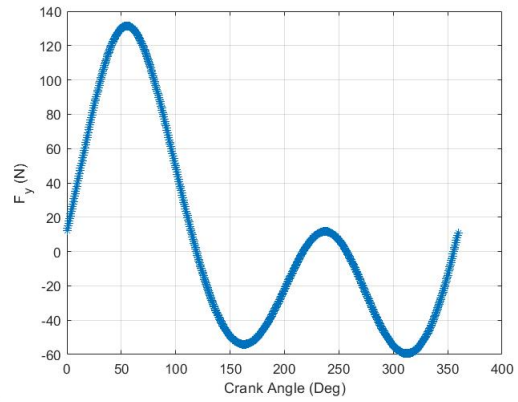
(b) $F_{Y''}(N)$
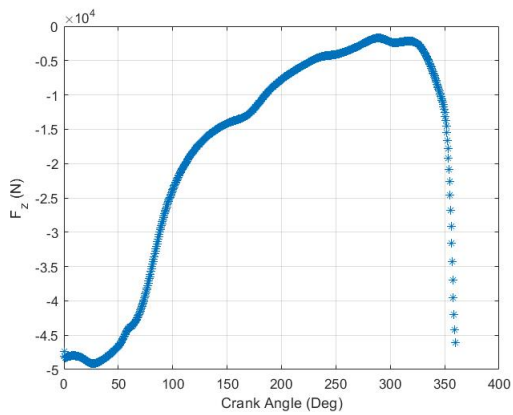
(c) $F_{Z''}(N)$

(d) $F_C(N)$

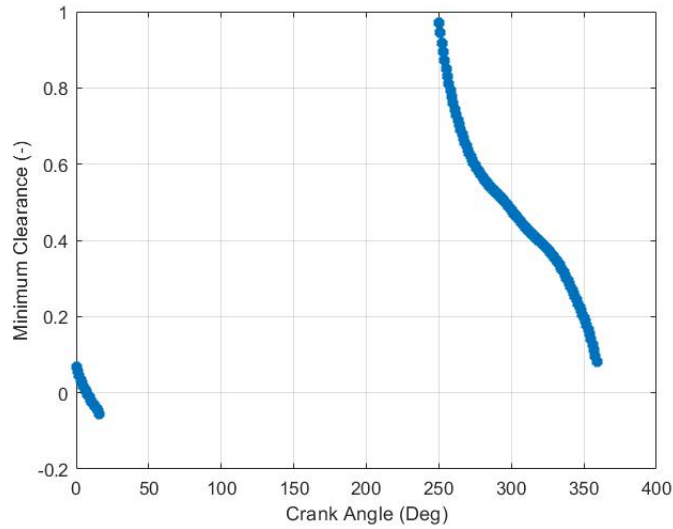Figure 6-1: Force on Ball in Socket Coordinate System (N)

Figure 6-2: Minimum clearance (-)

clearance is large. The initial conditions for the eccentricity parameter were set to be $(0.037, 0.037tan(20°), \pi)$. The initial condition for the non-dimensional minimum film thickness, h_{min} was assumed to be equal to the reference thickness, h_{ref}, such that $h_{min} = \frac{h}{h_{ref}} = 1$. The spatial coordinates of the maximum pressure were recorded as well as the clearance between the surface of the ball and the surface of the socket.

In figures 6-3 and 6-2, the non-dimensional pressure and minimum clearance are plotted against the crank angle between 250 and 15 degrees. It will be recalled from chapter 5 that the reference pressure is equal to $6.467 \times 10^5 Pa$ and the reference clearance is equal to $3.81 \times 10^{-5} m$.

From figure 6-3, the maximum pressure reaches roughly 300. Converting into dimensional units translates to $190 MPa$, or $28 ksi$. At this point, the minimum clearance drops below zero, indicating that the two surfaces have made contact. The hydrodynamic lubrication assumption that was initially made does not apply for this range and thus the results are invalid for calculating the amount of dissipated power due to friction. After 7 degrees, the minimum clearance drops below zero; results taken after 7 degrees will be considered invalid. Leading up to the point at which the minimum clearance drops below zero, the separate pieces of the dissipated friction power were plotted spatially over the θ and ϕ domain. Each contribution
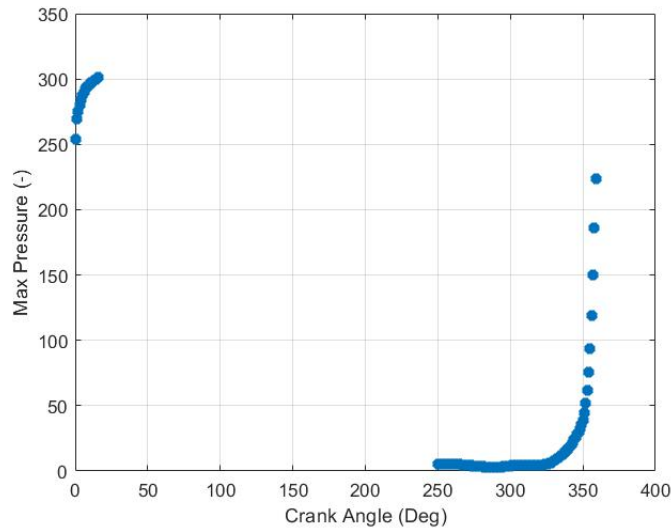
47

Figure 6-3: Maximum Pressure as a Function of Crank Angle (-)

from Poiseuille and Couette flow for both θ and ϕ directions were plotted individually, according to the definitions of $\dot{W}_1$, $\dot{W}_2$, $\dot{W}_3$, and $\dot{W}_4$ in chapter 5. Figures 6-4 through 6-7 show the individual contributions, and figure 6-8 shows the total sum of each component for the dissipated friction power across the domain as the crank angle advances from angle 5 degrees to angle 6 degrees.
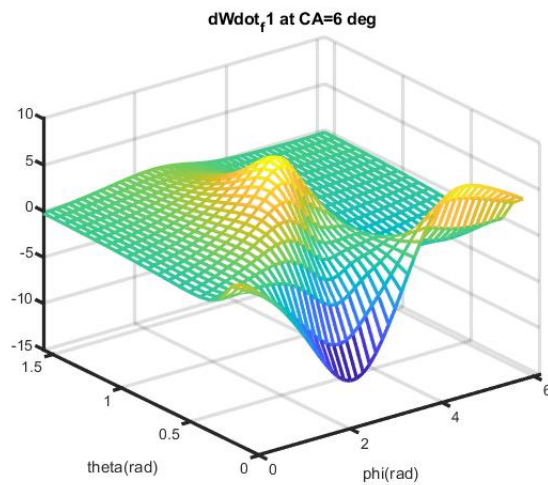

Figure 6-4: $d\dot{W}_1$ Spatial distribution at Crank Angle 6 degrees

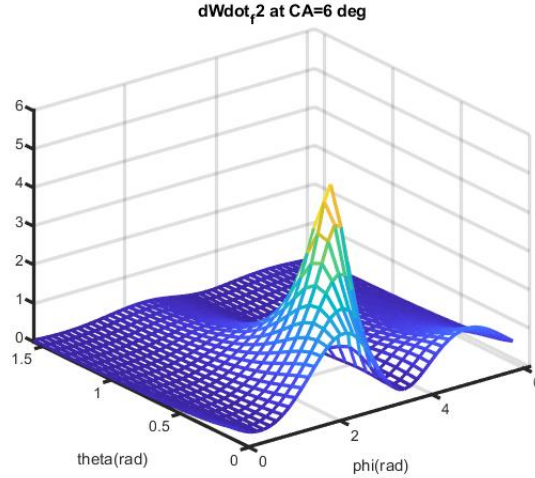Figures 6-4 and 6-6 are the Couette flow contributions in the θ and ϕ directions, respectively.

48

Figure 6-5: $d\dot{W}_2$ Spatial distribution at Crank Angle 6 degrees

Figure 6-5 and 6-7 are the Poiseuille flow contributions in the θ and ϕ directions, respectively. Poiseuille flow depends on the pressure gradient across the domain. If the change in pressure is negative, that implies the pressure goes from high to low, which is a positive pressure differential, ΔP. A positive pressure differential causes movement, and with movement induces a shear stress resisting the flow of the two surfaces against the fluid. The positive values of $d\dot{W}_2$ and $d\dot{W}_4$ indicate when there is a positive pressure differential, as the shear stress would oppose the motion of the ball against the fluid. A negative pressure differential indicates that the pressure is changing from low to high. A negative pressure differential opposes the line of motion. As the shear stress acts opposite to a negative pressure differential, the friction due to the shear stress aids the motion of the ball against the fluid.

From figure 6-8, the total dissipated friction power from contributions of $\dot{W}_1$, $\dot{W}_2$, $\dot{W}_3$, and $\dot{W}_4$ is $9.6W$ at 6 degrees crank angle. The program assumes infinite smoothness in the two surfaces. Even though the minimum clearance diminishes to be on the order of 0.001, or $0.038\mu m$, in this region, the assumption of hydrodynamic lubrication is still valid for the case of infinitely smooth surfaces. The dissipated power due to friction is negligible compared to the power extracted by the piston. Estimating the velocity to be $U_{ref} = 3.692\frac{m}{sec}$, the viscous friction force is $\frac{9.6W}{3.692\frac{m}{sec}} = 2.6N$. The force load is $4 \times 10^4 N$. The coefficient of friction is estimated to be on the order of
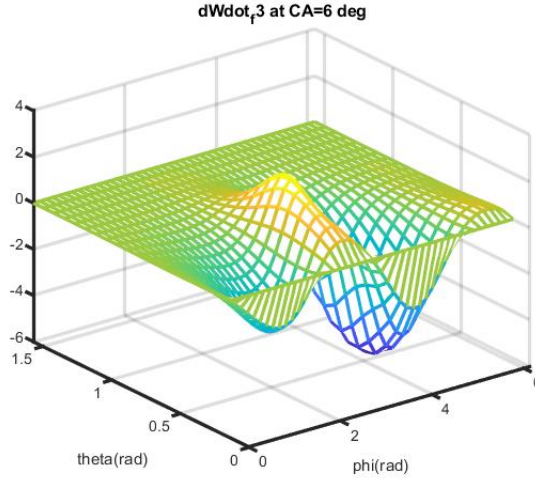
Figure 6-6: $d\dot{W}_3$ Spatial distribution at Crank Angle 6 degrees

$\frac{2.6N}{10^4 N} = 2.6 \times 10^{-4}$. Therefore, hydrodynamic friction is negligible. In reality, boundary lubrication is present when the clearance between the ball and socket is within the asperity of the surfaces.

Figure 6-9(a) shows the θ and ϕ locations for the contours of the pressure across the crank angle at 6 degrees. The maximum pressure point is roughly located at $\theta = 0.5rad$ and $\phi = 3.2rad$. Based on observations made during the study of the locations for the maximum pressure, it appears that the pressure is highly dependent on the θ location, rather than the ϕ location. Over the course of running the program from crank angles 250 degrees to 15 degrees, the recorded location of the max pressure did not change from $3.2rad$ in the ϕ direction, but varied significantly in the θ direction. This is likely due to the magnitude and direction of the force vector. Figure 6-1 shows that the dominating force is in the Z'' direction, along the axis of the oil hole. The main motion of the wobble plate is restricted to the $X'' - Z''$ plane due to the cam follower. Recall that θ is a measurement of the angle from the Z'' axis and ϕ is measured off of the X'' axis. The pressure dependence on the θ direction is expected. With a finer grid, it can be said that the ϕ coordinate does change with the crank angle, but the change is not expected to be significant. For comparison, a contour plot at an arbitrary crank angle equal to 331 degrees is shown in figure 6-9(b). This crank angle corresponds to a load of $3776.5N$. Referencing the figure, it can be seen that the
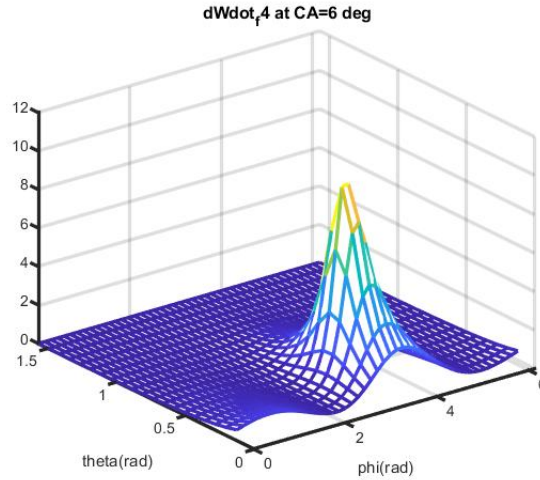
Figure 6-7: $d\dot{W}_4$ Spatial distribution at Crank Angle 6 degrees

maximum pressure is located at $\theta = 0.657rad$ and $\phi = 3.2rad$. The boundary of the oil hole in the socket was set to $\theta_0 = 0.125rad$. The pressure increases dramatically as it gets closer to the oil hole, transitioning into a concentrated spike. $\phi = 3.2rad$ is approximately 180 degrees, which corresponds to the $-X''$ axis of the SCS.

Figure 6-10 illustrates the pressure gradient for the θ direction across the domain of θ and ϕ. Figure 6-11 does the same for the ϕ direction. Comparing the vertical axes of the two figures further illustrates the magnitude of the pressure dependence on the θ direction, which can be confirmed by examining wear patterns in the socket.
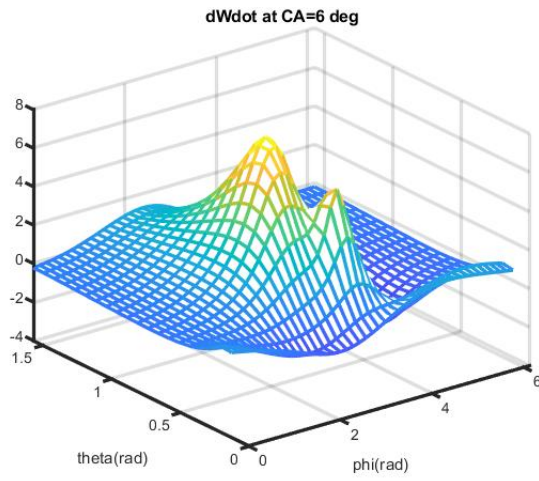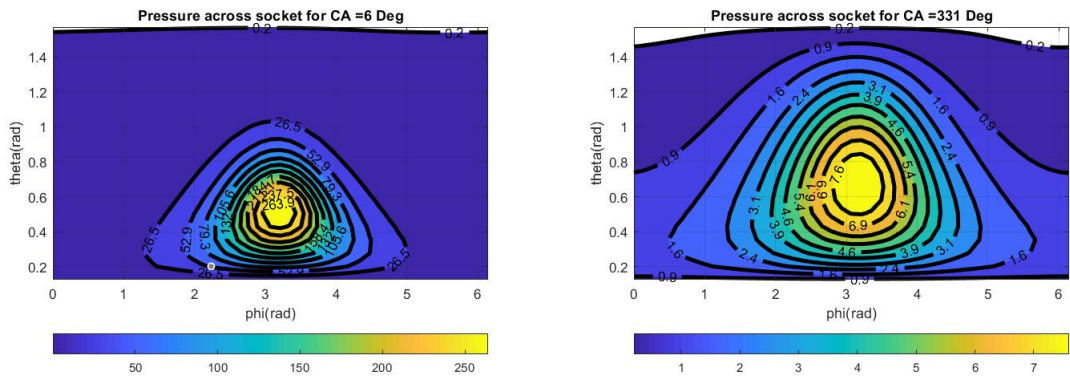
Figure 6-8: $d\dot{W}$ Spatial distribution at Crank Angle 6 degrees

(a) Crank Angle 6 Degrees

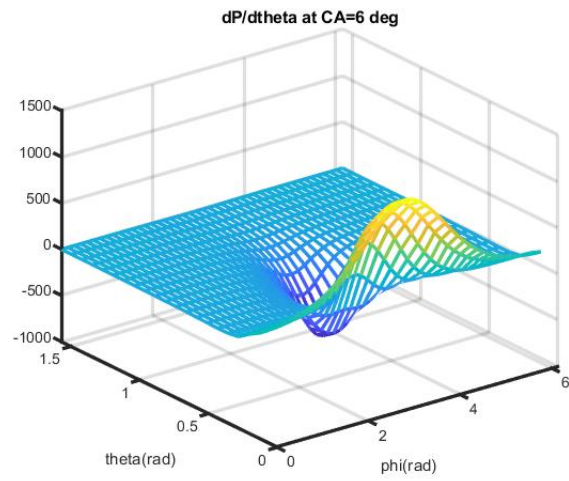(b) Crank Angle 331 Degrees

Figure 6-9: Pressure Contours

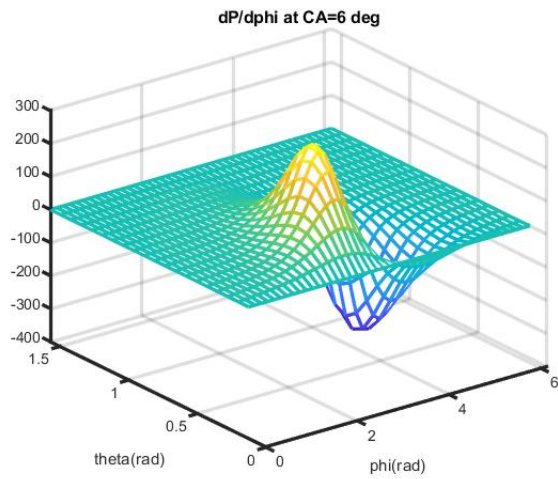Figure 6-10: Pressure Gradient in θ direction for Crank Angle 6 Degrees

Figure 6-11: Pressure Gradient in ϕ direction for Crank Angle 6 Degrees

Chapter 7

Conclusion

The results presented in chapter 6 show the ball-socket joint hydrodynamic lubrication behavior for the crank angles ranging from 250 degrees to 15 degrees. This specific range has been chosen as it encompasses the region of no load to maximum load. The maximum pressure location moves mostly as a function of θ only, and not with ϕ. The dominant pressure magnitude is consistent with the magnitude of the force in the Z'' direction. In socket coordinates, the forces in the X'' and Y'' directions are small compared to the Z'' direction, which corresponds to the centerline of the oil hole in the SCS. The wobble plate ss constricted to moving and rotating about the $X'' - Z''$ plane by the cam follower. The connecting rod motion is therefore mostly on the $X'' - Z''$ plane. The inclination of the connecting rod to the Z'' axis in the high load crank angle range is small. Therefore, the dominant force component is in the Z'' direction.

The results show that as the load point, the intersection of the load force vector and the socket, moves closer to the oil hole, the pressure increases exponentially, and the distribution narrows. The pressure gradient direction in the oil hole vicinity implies that the oil is being forced back into the oil hole, rather than being distributed to the socket for lubricating the joint. At roughly 8 degrees crank angle, the minimum clearance drops below zero; the two surfaces come into contact with each other and start to scrape against each other. Results beyond 7 degrees are considered invalid in this study, as the initial assumption for the program was fully hydrodynamic

lubrication. To incorporate boundary lubrication was outside the scope of this study.

The peak dissipated friction power for the range of crank angles between 250 degrees and 7 degrees was calculated to be $9.6W$. Using the relative ball-socket surface velocity, the hydrodynamic frictional force is estimated to be $2.6N$. The load force is $4 \times 10^4 N$. The frictional coefficient due to hydrodynamic friction between the two metal surfaces with oil lubrication is on the order of 10^{-4}, and is therefore negligible. This order of magnitude is consistent with the findings of reference [10]. It should be noted that, for crank angles 358 degrees to 7 degrees, the minimum non-dimensional clearance is on the order of 1×10^{-2} and 1×10^{-3} prior to the film thickness dropping below zero. In dimensional terms, this equated to roughly $3.7\mu m$ to as low as $0.082\mu m$. Because the surfaces have been assumed to be infinitely smooth, the presence of asperities is neglected. Taking an approximate height of large metal asperities to be roughly equal to $2\mu m$ [11], it is reasonable to assume that boundary lubrication occurs over the progression of the cycle. The power lost due to boundary friction will be much greater than what has been calculated in the 250 degree to 7 degree range. The power lost due to friction in the ball-socket joint of a swash plate engine is significantly lower than what has been seen in the interaction of pistons against the liner in a diesel engine, [12]. It is concluded that the dissipated power from hydrodynamic friction within the ball and socket joint is negligible for this scale of vehicle.

Bibliography

[1] A. G. Michell, "Crankless engine," Aug. 19 1930. US Patent 1,773,596.

[2] T. M. Cherry, "Anthony George Maldon Michell, 1870-1959," *The Royal Society*, 1962.

[3] R. Roberts and G. Brown, "A Complete Thermodynamic Analysis of a Swash-plate Piston Engine," Master's thesis, University of Rhode Island, 1987.

[4] X. Ai and H. S. Cheng, "Hydrodynamic Lubrication Analysis of a Metallic Hip Joint," *Tribology Transactions*, vol. 39, pp. 103–111, 1996.

[5] F. Hamano, "Derivative of rotation matrix direct matrix derivation of well known formula," *arXiv preprint arXiv:1311.6010*, 2013.

[6] B. Wie, *Space vehicle dynamics and control*. American Institute of Aeronautics and Astronautics, 2008.

[7] N. N. Janenko, *The method of fractional steps*. Springer, 1971.

[8] W. Lee, "Tridiagonal matrices: Thomas algorithm," *MS6021, Scientific Computation, University of Limerick*, 2011.

[9] D. Evans and S. Okolie, "A generalised sparse factorisation method for the solution of periodic tridiagonal systems," *Computers & Mathematics with Applications*, vol. 5, no. 3, pp. 211–216, 1979.

[10] S.-C. Vladescu, N. Marx, L. Fernández, F. Barceló, and H. Spikes, "Hydrodynamic friction of viscosity-modified oils in a journal bearing machine," *Tribology Letters*, vol. 66, no. 4, p. 127, 2018.

[11] F. Sun, E. Van der Giessen, and L. Nicola, "Effect of plastic flattening on the shearing response of metal asperities: a dislocation dynamics analysis," *Journal of Applied Mechanics*, vol. 82, no. 7, 2015.

[12] D. Singh, F. Gu, J. D. Fieldhouse, N. Singh, and S. Singal, "Prediction and analysis of engine friction power of a diesel engine influenced by engine speed, load, and lubricant viscosity," *Advances in Tribology*, vol. 2014, 2014.

Appendix A

Transformation Matrix from Cartesian to Polar Coordinates

Shown in figure A-1 is the polar coordinate system superimposed against the Cartesian coordinate system. The z axis represents the centerline of the socket. The x axis perpandicular to the z axis in line with the cam follower, and the y axis is dictated by the right hand rule,

$$\hat{y} = \hat{z} \times \hat{x}$$

In figure A-1, θ is defined as the angle measured from the vertical z axis, and ϕ is defined as the angle from the x axis.
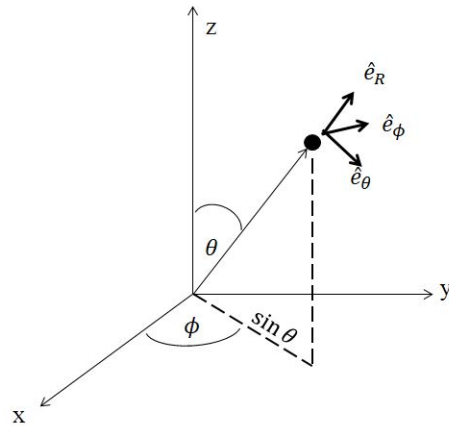

Figure A-1: Polar Coordinate System Against Cartesian

From figure A-1,

$$\hat{e}_\theta = cos\theta cos\phi \hat{x} + cos\theta sin\phi \hat{y} - sin\theta \hat{z}$$

$$\hat{e}_R = sin\theta cos\phi \hat{x} + sin\theta sin\phi \hat{y} + cos\theta \hat{z}$$

$\hat{e}_\phi$ is given by

$$\hat{e}_\phi = \hat{e}_R \times \hat{e}_\theta$$

$$\hat{e}_\phi = (sin\theta sin\phi \hat{y} + sin\theta cos\phi \hat{x} + cos\theta \hat{z}) \times (cos\theta cos\phi \hat{x} + cos\theta sin\phi \hat{y} - sin\theta \hat{z})$$

$$= -sin\phi \hat{x} + cos\phi \hat{y}$$

$$\begin{bmatrix} sin\theta & sin\theta sin\phi & cos\theta \\ cos\theta cos\phi & cos\theta sin\phi & -sin\theta \\ -sin\phi & cos\phi & 0 \end{bmatrix} \begin{bmatrix} \hat{x} \\ \hat{y} \\ \hat{z} \end{bmatrix} = \begin{bmatrix} \hat{e}_R \\ \hat{e}_\theta \\ \hat{e}_\phi \end{bmatrix}$$

where the transformation matrix between Cartesian and polar coordinates is equal to

$$T_{CtP} = \begin{bmatrix} sin\theta & sin\theta sin\phi & cos\theta \\ cos\theta cos\phi & cos\theta sin\phi & -sin\theta \\ -sin\phi & cos\phi & 0 \end{bmatrix}$$

Appendix B

Poisson Solver

The Reynolds equation in spherical coordinates is:

$$
\begin{aligned}
sin\theta\frac{\partial}{\partial\theta}(sin\theta\frac{h^3}{\mu}\frac{\partial P}{\partial\theta}) + \frac{\partial}{\partial\phi}(\frac{h^3}{\mu}\frac{\partial P}{\partial\phi}) - 6Rsin\theta[\frac{\partial}{\partial\theta}(sin\theta\cdot uh) \\
+ \frac{\partial}{\partial\phi}(vh)] - 12R^2sin^2\theta\frac{\partial h}{\partial t} = 0
\end{aligned}
\tag{B.1}
$$

Equation B.1 can be rewritten in the form of Poisson's equation:

$$
\frac{\partial}{\partial\theta}(f\frac{\partial P}{\partial\theta}) + \frac{\partial}{\partial\phi}(g\frac{\partial P}{\partial\phi}) = Q
\tag{B.2}
$$

where

$$
\begin{aligned}
Q &= 6R[\frac{\partial}{\partial\theta}(sin\theta uh) + \frac{\partial}{\partial\phi}(vh)] + 12R^2 sin\theta\dot{h} \\
f &= sin\theta\frac{f^3}{\mu} \\
g &= \frac{1}{sin\theta}\frac{h^3}{\mu}
\end{aligned}
$$

The Method of Fractional Steps developed by Professor N.N. Yanenko was used to solve the parabolic equation shown in equation B.2 using a fixed pseudo time step. A weighted splitting scheme identified in reference [7] was used to solve Poisson's equation for the pressure over a fixed pseudo time step.

$$\frac{\partial P}{\partial \tau} = \frac{\partial}{\partial \theta}(sin\theta \frac{h^3}{\mu}\frac{\partial P}{\partial \theta}) + \frac{1}{sin\theta}\frac{\partial}{\partial \phi}(\frac{h^3}{\mu}\frac{\partial P}{\partial \phi}) - Q \qquad \text{(B.3)}$$

For every time, t, an initial guess equal to the previous value plus the previous increment is used film thickness, h. $\dot{h}$ is approximated by $\frac{h - h_{previous}}{\Delta t}$. This value is used to calculate the steady state value in the pseudo time, τ, for P from equation B.3. The pressure is integrated over the area to find the force.

Let i and j be the indices for the θ and ϕ coordinates, respectively. For an $M \times N$ grid in the θ and ϕ directions, the values of θ and ϕ are defined accordingly as

$$\Delta\theta = \frac{(\frac{\pi}{2} - \theta_0)}{M - 1}$$

$$\theta_i = (i - 1)\Delta\theta + \theta_0$$

$$\Delta\phi = \frac{2\pi}{N}$$

$$\phi_j = (j - 1)\Delta\phi$$

The terms in Q in difference form are

$$(\frac{\partial}{\partial \theta}(sin\theta uh))_{i,j} = \frac{(sin\theta uh)_{i+1,j} - (sin\theta uh)_{i-1,j}}{2\Delta\theta} \qquad \text{for } i = 2, M; \, j = 1, N$$

$$\frac{(sin\theta uh)_{2,j} - (sin\theta uh)_{1,j}}{\Delta\theta} \qquad \text{for } i = 1, \, j = 1, N$$

$$\frac{(sin\theta uh)_{M,j} - (sin\theta uh)_{M-1,j}}{\Delta\theta} \qquad \text{for } i = M, \, j = 1, N$$

$$(\frac{\partial}{\partial \phi}(vh))_{i,j} = \frac{(vh)_{i,j+1} - (vh)_{i,j-1}}{2\Delta\phi} \qquad \text{for } j = 2, N - 1; \, i = 1, M$$

$$\frac{(vh)_{i,2} - (vh)_{i,N}}{2\Delta\phi} \qquad \text{for } j = 1; \, i = 1, M$$

$$\frac{(vh)_{i,1} - (vh)_{i,N-1}}{2\Delta\phi} \qquad \text{for } j = N; \, i = 1, M$$

$$Q_{i,j} = 6R([\frac{\partial}{\partial\theta}(sin\theta uh)]_{i,j} + \frac{1}{sin\theta_i}[\frac{\partial}{\partial\phi}(vh)]_{i,j}) + 12R^2 sin\theta_i \dot{h}_{i,j}$$

The first term in Q is calculated using one sided efficiency for the edge points. The middle and third terms in Q are calculated using one-sided efficiency and periodic boundary conditions.

Using the weighted splitting scheme for a fixed pseudo time step, equation B.3 can be broken into two steps

$$\frac{P^{n+\frac{1}{2}} - P^n}{\frac{1}{2}\Delta\tau} = \frac{\partial}{\partial\theta}(sin\theta\frac{h^3}{\mu}\frac{\partial P^{n+\frac{1}{2}}}{\partial\theta}) + \frac{1}{sin\theta}\frac{\partial}{\partial\phi}(\frac{h^3}{\mu}\frac{\partial P^n}{\partial\phi}) - Q \qquad \text{(B.4)}$$

$$\frac{P^{n+1} - P^{n+\frac{1}{2}}}{\frac{1}{2}\Delta\tau} = \frac{\partial}{\partial\theta}(sin\theta\frac{h^3}{\mu}\frac{\partial P^{n+\frac{1}{2}}}{\partial\theta}) + \frac{1}{sin\theta}\frac{\partial}{\partial\phi}(\frac{h^3}{\mu}\frac{\partial P^{n+1}}{\partial\phi}) - Q \qquad \text{(B.5)}$$

For any function, $y = f(x)$, a second order approximation in Δx can be written in the following form:

$$\frac{\partial}{\partial x}[f\frac{(\partial y)}{\partial x}] \qquad\qquad\qquad \text{to 2nd order in } \Delta x$$

$$= \frac{(f\frac{\partial y}{\partial x})_{i+\frac{1}{2}} - (f\frac{\partial y}{\partial x})_{i-\frac{1}{2}}}{\Delta x}$$

$$= (\frac{f_i + f_{i+1}}{2})(\frac{y_{i+1} - y_i}{\Delta x^2}) - (\frac{f_i + f_{i-1}}{2})(\frac{y_i - y_{i-1}}{\Delta x^2})$$

Using the definitions of f and g previously defined, and applying to equations B.4 and B.5, equation B.4 becomes

$$\frac{P_{i,j}^{n+\frac{1}{2}} - P_{i,j}^n}{\frac{1}{2}\Delta\tau} = \frac{f_{i,j} + f_{i+1,j}}{2}\frac{P_{i+1,j}^{n+\frac{1}{2}} - P_{i,j}^{n+\frac{1}{2}}}{(\Delta\theta)^2} - \frac{f_{i,j} + f_{i-1,j}}{2}\frac{P_{i,j}^{n+\frac{1}{2}} - P_{i-1,j}^{n+\frac{1}{2}}}{(\Delta\theta)^2}$$

$$+ \frac{(g_{i,j+1} + g_{i,j})}{2}\frac{(P_{i,j+1}^n - P_{i,j}^n)}{(\Delta\phi)^2} - \frac{(g_{i,j} + g_{i,j-1})}{2}\frac{(P_{i,j}^n - P_{i,j-1}^n)}{(\Delta\phi)^2}$$

$$- Q_{i,j}$$

Note that this applies for $i = 2, ..., M - 1$ and for $j = 1, ...N,$. The pressures at the boundaries, P_1 and P_M, are constants that are given. Note that for the case of the

periodic boundaries, at $j = N + 1$, the values at $j = 1$ are used and at $j = 0$, the values at $j = N$ are used.

Collecting and rearranging terms such that

$$-A_i y_{i+1} + B_i y_i - C_i y_{i-1} = D_i$$

where $y_i = P_{i,j}^{n+\frac{1}{2}}$.

$$D_{i,j} = [(\frac{g_{i,j+1} + g_i, j}{2}) \frac{(P_{i,j+1}^n - P_{i,j}^n)}{(\Delta\phi)^2} - \frac{(g_{i,j} + g_{i,j-1})}{2} (\frac{P_{i,j}^n - P_{i,j-1}^n}{(\Delta\phi)^2}) - Q_{i,j}]$$

$$B_{i,j} = 1 + (\frac{f_{i,j} + f_{i+1,j}}{2}) \frac{\frac{\delta\tau}{2}}{(\Delta\theta)^2} + (\frac{f_{i,j} + f_{i-1,j}}{2}) \frac{\frac{\delta\tau}{2}}{(\Delta\theta)^2}$$

$$= 1 + \frac{\delta\tau}{2(\Delta\theta)^2} [f_{i,j} + \frac{1}{2} f_{i+1,j} + \frac{1}{2} f_{i-1,j}]$$

$$A_{i,j} = (\frac{f_{i,j} + f_{i+1,j}}{2}) \frac{\frac{1}{2}\delta\tau}{(\Delta\theta)^2}$$

$$C_{i,j} = (\frac{f_{i,j} + f_{i-1,j}}{2}) \frac{\frac{1}{2}\delta\tau}{(\Delta\theta)^2}$$

The variables, $A_{i,j}$, $B_{i,j}$, $C_{i,j}$, and $D_{i,j}$ are defined for $i = 2, ..., M - 1$. The values for $A_{1,j}$ and $A_{M,j}$ are never used in the program.

Using the defined parameters and having rewritten Poisson's equation in terms of a weighted splitting scheme, the variables can be arranged such that the Modified Thomas Algorithm can be used to solve for the pressure. As written previously,

$$-A_i y_{i+1} + B_i y_i - C_i y_{i-1} = D_i \qquad \text{for } i = 2, ..., M - 1$$

Let

$$y_i = E_i y_{i+1} + F_i \tag{B.6}$$

Then

$$-A_i y_{i+1} + B_i y_i - C_i(E_{i-1} y_i + F_{i-1}) = D_i$$

or $-A_i y_{i+1} + (B_i - C_i E_{i-1}) y_i - C_i F_{i-1} = D_i$. Rearranging and solving for the previous iteration

$$y_i = \left(\frac{A_i}{B_i - C_i E_{i-1}}\right) y_{i+1} + \frac{D_i + C_i F_{i-1}}{B_i - C_i E_{i-1}}$$

Comparing with (B.6) gives

$$E_i = \frac{A_i}{B_i - C_i E_{i-1}}$$
$$F_i = \frac{D_i + C_i F_{i-1}}{B_i - C_i E_{i-1}}$$

which is valid for $i = 2, ...M - 1$. These variables are defined for a forward step in pseudo time. Given initial boundary conditions, $E_1 = 0$ and $F_1 = y_1$. The backward sweep is given by y_m,

$$y_{i-1} = E_{i-1} y_i + F_{i-1}$$

B.1 Matrix Formulation

The equations can be rewritten in matrix form and be easily solved in MATLAB

$$\begin{bmatrix} -C_2 & B_2 & A_2 & 0 & \cdots \\ & \ddots & \ddots & & \\ & & -C_{M-1} & B_{M-1} & A_{M-1} \end{bmatrix} \begin{bmatrix} y_1 \\ y_2 \\ y_3 \\ \cdots \\ y_{M-1} \\ y_M \end{bmatrix} = \begin{bmatrix} D_2 \\ D_3 \\ \cdots \\ D_{M-1} \end{bmatrix}$$

Augmented by y_1 and y_M are given as Boundary Conditions, then

$$\begin{bmatrix} 1 & 0 & 0 & \ldots & & 0 \\ 0 & -C_2 & B_2 & A_2 & \ldots & 0 \\ 0 & & \ddots & \ddots & & \\ \vdots & & & -C_{M-1} & B_{M-1} & A_{M-1} \\ 0 & 0 & \ldots & & & 1 \end{bmatrix} \begin{bmatrix} y_1 \\ y_2 \\ y_3 \\ \ldots \\ y_{M-1} \\ y_M \end{bmatrix} = \begin{bmatrix} y_1 \\ D_2 \\ D_3 \\ \ldots \\ D_{M-1} \\ y_M \end{bmatrix}$$

The sparse matrix in the i direction, S_θ, is defined as

$$S_\theta = \begin{bmatrix} 1 & 0 & 0 & \ldots & & 0 \\ 0 & -C_2 & B_2 & A_2 & \ldots & 0 \\ 0 & & \ddots & \ddots & & \\ \vdots & & & -C_{M-1} & B_{M-1} & A_{M-1} \\ 0 & 0 & \ldots & & & 1 \end{bmatrix}$$

which has dimensions of $M \times M$. The elements of the sparse matrix will be defined by $v(i,j)$. For $i = 1$ and $i = M$

i	j	$v(i,j)$
1	1	1
M	M	1

For $i = 2$ to $i = M = 1$

$$\begin{array}{l|l} j = i & v(i,j) = B_i \\ j = i - 1 & v(i,j) = -C_i \\ j = i + 1 & v(i,j) = -A_i \end{array}$$

Then

$$
\begin{bmatrix} y_1 \\ y_2 \\ y_3 \\ \dots \\ y_{M-1} \\ y_M \end{bmatrix} = S^{-1} \begin{bmatrix} y_1 \\ D_2 \\ D_3 \\ \dots \\ D_{M-1} \\ y_M \end{bmatrix}
$$

B.2 Fractional Step with Periodic Boundary Conditions

In the previous section, equation B.4 was solved for using the Modified Thomas Algorithm. This section will show how the second half fractional step, equation B.5 is solved for the pressure in the ϕ direction. Note that the pressure in the ϕ direction has periodic boundary conditions, and that the points $j = N + 1$ and $j = 1$ are the same. Recall that equation B.5 is:

$$
\frac{P^{n+1} - P^{n+\frac{1}{2}}}{\frac{1}{2}\Delta\tau} = \frac{\partial}{\partial\theta}(sin\theta\frac{h^3}{\mu}\frac{\partial P^{n+\frac{1}{2}}}{\partial\theta}) + \frac{1}{sin\theta}\frac{\partial}{\partial\phi}(\frac{h^3}{\mu}\frac{\partial P^{n+1}}{\partial\phi}) - Q
$$

The second order approximation of $\frac{\partial}{\partial x}[f\frac{(\partial y)}{\partial x}]$ was again used for equation B.5 to produce

$$
\begin{aligned}
\frac{P_{i,j}^{n+1} - P_{i,j}^{n+\frac{1}{2}}}{\frac{1}{2}\Delta\tau} =& (\frac{f_{i,j} + f_{i+1,j}}{2})(\frac{P_{i+1,j}^{n+\frac{1}{2}} - P_{i,j}^{n+\frac{1}{2}}}{\Delta\theta^2}) \\
& - (\frac{f_{i,j} + f_{i-1,j}}{2})(\frac{P_{i,j}^{n+\frac{1}{2}} - P_{i-1,j}^{n+\frac{1}{2}}}{\Delta\theta^2}) \\
& + \frac{(g_{i,j+1} + g_{i,j})}{2}\frac{(P_{i,j+1}^{n+1} - P_{i,j}^{n+1})}{(\Delta\phi)^2} - \frac{(g_{i,j} - g_{i,j-1})}{2}\frac{(P_{i,j}^{n+1} - P_{i,j-1}^{n+1})}{(\Delta\phi)^2} \\
& - Q_{i,j}
\end{aligned}
$$

Defining $z_j = P_{i,j}^{n+1}$ and suppressing subscript i and superscript $i + 1$,

67

$$-a_{i,j}z_{j+1} + b_j z_j - c_j z_{j-1} = d_j$$

Then

$$d_{i,j} = (\frac{f_{i,j} + f_{i+1,j}}{2})\frac{\frac{1}{2}\Delta\tau}{(\Delta\theta)^2}(P_{i+1,j}^{n+\frac{1}{2}} - P_{i,j}^{n+\frac{1}{2}}$$
$$- \frac{(f_{i,j} + f_{i-1,j})}{2}\frac{\frac{1}{2}\Delta\tau}{(\Delta\theta)^2}(P_{i,j}^{n+\frac{1}{2}} - P_{i-1,j}^{n+\frac{1}{2}})$$
$$- Q_{i,j}\frac{\Delta\tau}{2} + P_{i,j}^{n+\frac{1}{2}}$$

for $i = 2, ..., M - 1$, since the pressure at the boundaries, P_1 and P_M, are given constants.

$$b_{i,j} = 1 + \frac{g_{i,j+1} + g_{i,j}}{2}\frac{\frac{1}{2}\Delta\tau}{(\Delta\phi)^2} + \frac{g_{i,j} + g_{i,j-1}}{2}\frac{\frac{1}{2}\Delta\tau}{(\Delta\phi)^2}$$
$$= 1 + \frac{\frac{1}{2}\Delta\tau}{(\Delta\phi)^2}\frac{(g_{i,j+1} + g_{i,j-1}}{2} + g_{i,j})$$

$$a_{i,j} = \frac{(g_{i,j+1} + g_{i,j}}{2}\frac{\delta\tau}{2(\Delta\phi)^2}$$

$$c_{i,j} = \frac{g_{i,j-1} + g_{i,j}}{2}\frac{\delta\tau}{2(\Delta\phi)^2}$$

for $j = 1, N$. Because of the periodic boundaries, for $j = N + 1$ the value at $j = 1$ can be used.

The parameters can be defined in matrix form and the Modified Thomas Algorithm can be used to solve for the coefficients.

$$\begin{bmatrix} b_1 & -a_1 & 0 & \ldots & & -c_1 \\ -c_2 & b_2 & a_2 & 0 & \ldots & \\ 0 & \ddots & \ddots & \ddots & & 0 \\ \vdots & & \ddots & \ddots & & \ddots \\ 0 & & & -c_{N-1} & b_{N-1} & -a_{N-1} \\ -a_N & & & & -c_N & b_N \end{bmatrix} \begin{bmatrix} z_1 \\ \vdots \\ z_N \end{bmatrix} = \begin{bmatrix} d_1 \\ \vdots \\ d_N \end{bmatrix}$$

As before, the sparse matrix, S_ϕ is defined as

$$
S_\phi =
\begin{bmatrix}
b_1 & -a_1 & 0 & \cdots & & -c_1 \\
-c_2 & b_2 & a_2 & 0 & \cdots & \\
0 & \ddots & \ddots & \ddots & & 0 \\
\vdots & & \ddots & \ddots & & \ddots \\
0 & & & -c_{N-1} & b_{N-1} & -a_{N-1} \\
-a_N & & & & -c_N & b_N
\end{bmatrix}
$$

In this case, S_ϕ has dimensions of $N \times N$. Similarly to S_θ, S_ϕ can be defined by the values $v(i,j)$

$$
\begin{array}{c|c}
j = i & v(i,j) = b_i \\
j = i - 1 & v(i,j) = -c_i \\
j = i + 1 & v(i,j) = -a_i
\end{array}
$$

for $i = 2 : N - 1$.

$$
\begin{array}{c|c}
j = 1 & v = b_1 \\
j = N & v = -c_1 \\
j = 2 & v = -a_1
\end{array}
$$

for $i = 1$.

$$
\begin{array}{c|c}
j = 1 & v = b_N \\
j = N - 1 & v = -c_N \\
j = N & v = -a_N
\end{array}
$$

for $i = N$.

Appendix C

Dissipated Friction Power

The Navier-Stokes equation was reduced to solve for the velocity gradients in each of the θ and ϕ directions. The origin of the coordinate system was set to be at the center of the socket, in the socket coordinate system. For the θ direction,

$$\frac{1}{\mu R}\frac{\partial P}{\partial \theta} = \frac{1}{R^2}\frac{\partial}{\partial y}(R^2\frac{\partial u}{\partial y})$$
$$= \frac{\partial^2 u}{\partial y^2}$$

and the ϕ direction:

$$\frac{1}{\mu R sin\theta}\frac{\partial P}{\partial \phi} = \frac{1}{R^2}\frac{\partial}{\partial y}(R^2\frac{\partial v}{\partial y})$$
$$= \frac{\partial^2 v}{\partial y^2}$$

The boundary conditions are defined in table C.1. At the surface of the socket, the no slip boundary condition is applied. At the surface of the ball, the θ and ϕ velocities are equal to constant velocities U and V.

| $u = 0$ | $v = 0$ | $y = 0$ |
| $u = U$ | $v = V$ | $y = h$ |

Table C.1: Boundary Conditions

Solving for the velocity distribution for both directions with the identified boundary conditions yields

$$u(y) = \frac{1}{\mu R}\frac{\partial P}{\partial \theta}[y^2 - hy] + \frac{U}{h}y \tag{C.1}$$

$$v(y) = \frac{1}{2\mu R sin\theta}\frac{\partial P}{\partial \phi}[y^2 - hy] + \frac{V}{h}y \tag{C.2}$$

Equations C.1 and C.2 were integrated over the film thickness to find an expression for the bulk velocities, $\bar{u}$, $\bar{v}$.

$$\bar{u} = \int_0^h u\,dy = \frac{1}{12\mu R}(-\frac{\partial P}{\partial \theta})h^3 + \frac{Uh}{2} \tag{C.3}$$

$$\bar{v} = \int_0^h v\,dy = \frac{1}{12\mu R sin\theta}(-\frac{\partial P}{\partial \phi})h^3 + \frac{Vh}{2} \tag{C.4}$$

Let the viscous stress be denoted by $\tau_{i,j}$ where i and j represent the direction of the shear stress according to the shear tensor. As an example, $\tau_{\theta,R}$ is the shear stress that acts in the θ direction, perpendicular to the R direction.

$$\tau_{\theta,R} = \mu\frac{\partial u}{\partial y}$$
$$\tau_{\phi,R} = \mu\frac{\partial v}{\partial y}$$

Using the definition of the bulk velocities calculated in equations C.3 and C.4, the shear stress in the θ and ϕ directions is equal to:

$$\tau_{\theta,R} = \frac{h}{2R}\frac{\partial P}{\partial \theta} + \frac{\mu U}{h}$$
$$\tau_{\phi,R} = \frac{h}{R sin\theta}\frac{\partial P}{\partial \phi} + \frac{\mu V}{h}$$

The change in the dissipated friction power per area is equal to

$$\frac{d\dot{W}_f}{dA} = (\tau_{\theta,R})u + (\tau_{\phi,R})v \tag{C.5}$$

The total dissipated friction power is calculated by integrating over the domain:

$$\dot{W}_f = \int_A \frac{d\dot{W}_f}{dA} dA$$
$$= \int_0^{2\pi} \int_{\theta_0}^{\frac{\pi}{2}} (\frac{d\dot{W}_f}{dA}) R^2 sin\theta d\theta d\phi \tag{C.6}$$

Expanding $\frac{d\dot{W}_f}{dA}$ from equation C.5 gives:

$$\frac{d\dot{W}_f}{dA} = [\frac{hU}{2R}(-\frac{\partial P}{\partial\theta}) + \frac{\mu U^2}{h}] + [\frac{hV}{2Rsin\theta}(-\frac{\partial P}{\partial\phi}) + \frac{\mu V^2}{h}] \tag{C.7}$$

The variables calculated in the Poisson solver in chapter 5 uses strictly non-dimensional terms. The parameters shown in C.7 have dimensions. They are non-dimensionalized as shown in table C.2. The starred values have no dimensions.

P	$P_{ref}P^*$
R	$R_{ref}R^*$
h	$H_{ref}h^*$
U	$U_{ref}u^*$
V	$U_{ref}v^*$

Table C.2: Non-Dimensional Parameters

Recall that $P_{ref} = \mu R_{ref}\frac{U_{ref}}{H_{ref}^2}$. Inserting the non-dimensional substitutes from table C.2 into equation C.7 gives

$$P_{ref}\frac{H_{ref}U_{ref}}{R_{ref}}(\frac{h^*U^*}{2R^*}(-\frac{\partial P^*}{\partial\theta})) + (\frac{U_{ref}^2}{H_{ref}})(\frac{\mu u^{*2}}{h^2})$$
$$+ \frac{H_{ref}U_{ref}P_{ref}}{R_{ref}}(\frac{h^*v^*}{2R^*sin\theta})(-\frac{\partial P^*}{\partial\phi}) + \frac{U_{ref}^2}{H_{ref}}(\frac{\mu v^{*2}}{h^*})$$

The constant $P_{ref}\frac{H_{ref}U_{ref}}{R_{ref}}$ when expanded using the definition of P_{ref} is equal to $\mu\frac{U_{ref}^2}{H_{ref}}$. Factoring out the common multiple gives:

$$\frac{d\dot{W}_f}{dA} = P_{ref}\frac{H_{ref}U_{ref}}{R_{ref}}[\frac{h^*u^*}{2R^*}(-\frac{\partial P^*}{\partial\theta}) + \frac{u^{*2}}{h^*} + \frac{h^*v^*}{2R^*sin\theta}(-\frac{\partial P^*}{\partial\phi}) + \frac{v^{*2}}{h^*}] \tag{C.8}$$

Using this expression for $\frac{d\dot{W}_f}{dA}$ in equation C.6 yields the following result, which is

73

used in chapter 5 for calculating the dissipated friction power.

$$\dot{W}_f = \int_0^{2\pi} \int_{\theta_0}^{\frac{\pi}{2}} P_{ref} \frac{H_{ref}U_{ref}}{R_{ref}} [\frac{h^*u^*}{2R^*}(-\frac{\partial P^*}{\partial \theta}) + \frac{u^{*2}}{h^*} \\ + \frac{h^*v^*}{2R^*sin\theta}(-\frac{\partial P^*}{\partial \phi}) + \frac{v^{*2}}{h^*}]R^2 sin\theta d\theta d\phi \tag{C.9}$$